

Feature Learning beyond the Lazy-Rich Dichotomy: Insights from Representational Geometry

Chi-Ning Chou^{*1}, Hang Le^{*1}, Yichen Wang^{1,2}, and SueYeon Chung^{1,3}

¹Center for Computational Neuroscience, Flatiron Institute, New York, NY, USA.

²University of California, UCLA, Los Angeles, CA, USA

³Center for Neural Science, New York University, New York, NY, USA.

Abstract

The ability to integrate task-relevant information into neural representations is a fundamental aspect of both biological and artificial intelligence. To enable theoretical analysis, recent work has examined whether a network learns task-relevant features (*rich* learning) or resembles a random feature model (or a kernel machine, i.e., *lazy* learning). However, this simple lazy-versus-rich dichotomy overlooks the possibility of various subtypes of feature learning that emerge from different architectures, learning rules, and data properties. Furthermore, most existing approaches emphasize weight matrices or neural tangent kernels, limiting their applicability to neuroscience because they do not explicitly characterize representations—the fundamental units through which biological neural circuits encode and manipulate information.

In this work, we introduce an analysis framework based on representational geometry to study feature learning. Instead of analyzing what are the learned features, we focus on characterizing how task-relevant representational manifolds evolve during the learning process. In both theory and experiment, we find that when a network learns features useful for solving a task, the task-relevant manifolds become increasingly untangled. Moreover, by tracking changes in the underlying manifold geometry, we uncover distinct learning stages throughout training, as well as different learning strategies associated with training hyperparameters, uncovering subtypes of feature learning beyond the lazy-versus-rich dichotomy. Applying our method to neuroscience and machine learning, we gain geometric insights into the structural inductive biases of neural circuits solving cognitive tasks and the mechanisms underlying out-of-distribution generalization in image classification. Our framework provides a novel geometric perspective for understanding and quantifying feature learning in both artificial and biological neural networks.

1 Introduction

Learning induces changes in brain activity, whether it involves navigating a new city, adapting novel motor skills, or solving new cognitive tasks. These changes are reflected in the incorporation of task-relevant features into neural representations (Olshausen and Field, 1996; Poort et al., 2015; Niv, 2019; Reinert et al., 2021; Gurnani and Gajic, 2023). Similarly, the remarkable success of deep learning is often attributed to the ability of neural networks to learn problem-specific features¹.

*These authors contributed equally as first authors. Contact: {cchou, hle, chung}@flatironinstitute.org

¹Different papers and communities might treat the definition of *features* differently. In this paper, we adopt a more general way of thinking about features as measurable properties or characteristics of patterns in data/input represented by neural activity patterns.

For example, in deep neural networks (DNNs) (LeCun et al., 1998; Krizhevsky et al., 2012), the ability to learn rich feature hierarchies enables superior image classification performance (Girshick et al., 2014). Meanwhile, the seminal work of Chizat et al. (Chizat et al., 2019) demonstrated that neural networks can perform well even when there are negligible changes in the weights of the networks. These observations raise important questions: Do neural networks always need to learn task-relevant features? How can we evaluate the quality of the features they learn?

To answer these questions, researchers in representation learning have developed several methods to determine whether a neural network operates in the *lazy* regime (learning without changing internal features) or the *rich* regime (learning task-relevant features)². These methods include measuring changes in the weights of the network, tracking activated neurons, and assessing differences in the linearized model (also known as the neural tangent kernel, NTK (Jacot et al., 2018)). Factors such as initial weight norm, learning rate, and readout weight have been found to play a role in whether a network is lazy or rich (Chizat et al., 2019). Moreover, recent theoretical evidence has suggested that networks could perform better in the rich regime compared to the lazy regime (Yang and Hu, 2021; Shi et al., 2022; Karp et al., 2021; Damian et al., 2022; Ba et al., 2022).

However, feature learning is much *richer* than the lazy versus rich dichotomy. For example, changes in representations are not always beneficial as they can lead to issues such as catastrophic forgetting (Kirkpatrick et al., 2017). Moreover, different network architectures, training procedures, and objective functions, initializations, can result in different inductive biases for feature learning (Chizat et al., 2019; Bordelon and Pehlevan, 2022; Ba et al., 2022; Damian et al., 2022), yet all of these scenarios could fall under the broad category of rich learning. Lastly, current limitations in neuroscience technology for precisely tracking synaptic weight changes in neural circuits necessitate a framework based on neural representations rather than network weights or neural tangent kernel.

1.1 Contributions

In this work, we go beyond the lazy versus rich dichotomy and address the above-mentioned gaps by investigating feature learning through the geometric properties of task-relevant manifolds. Here, task-relevant manifolds refer to the point clouds of neural activity patterns that are related to the tasks. For example, in a classification task, a manifold could be the point cloud of neural activations corresponding to stimuli in a given category (e.g., the cat and dog manifolds in Figure 1a, left). In other domains, a manifold could correspond to a context (e.g., environmental cues) in a neuroscience experiment or to a concept (e.g., semantic categories) in a language model.

In a network that does not learn task-relevant features (e.g., lazy learning, random features, Figure 1b, left), the manifolds are poorly organized, making them harder to distinguish (e.g., smaller margin, smaller solution volume). In contrast, when a network learns task-relevant features (e.g., rich learning, neural collapse Figure 1b, right), the manifolds become well-organized and easier to separate (e.g., larger margin, larger solution volume). From this perspective, feature learning can be viewed as a process of *untangling* task-relevant manifolds—structuring the neural representational space to improve separation among manifolds.

To make this intuition concrete and quantitative, we propose the usage of *manifold capacity* (Chung et al., 2018; Chou et al., 2025) to quantify the degree of richness in feature learning (Figure 1c, left). Specifically, manifold capacity (Definition 2.1 and Definition B.3) quantifies the degree of manifold untangling via an average-case notion of how separable the manifolds are: manifold packability³. Additionally, manifold capacity is analytically connected to a collection of

²These two regimes are also known as *kernel regime* and *feature learning regime*.

³We remark that the margin in support vector machine (SVM) theory quantifies the degree of separability in

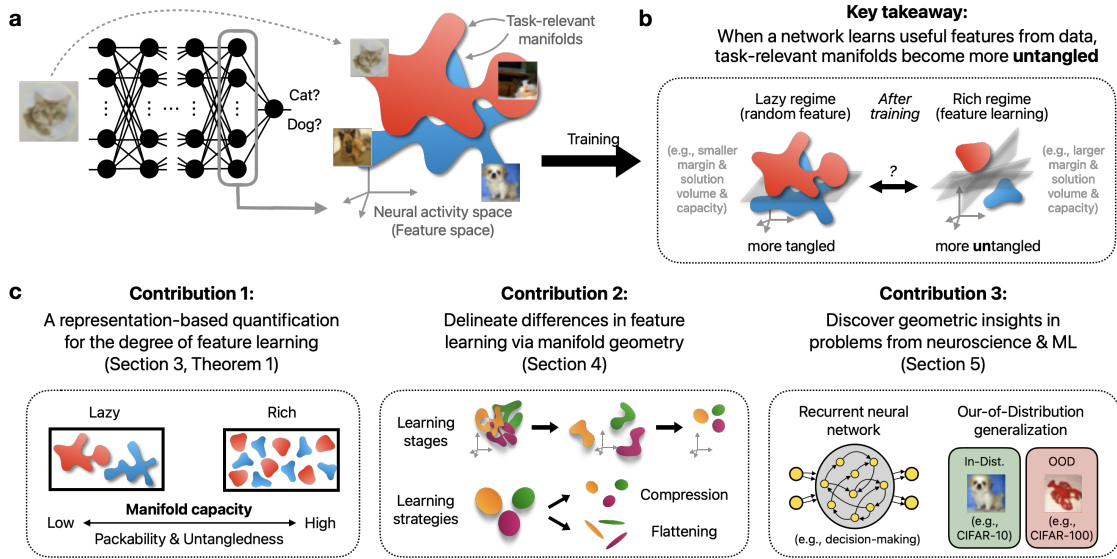


Figure 1: Schematic illustration. **a**, We propose to investigate feature learning via the geometry of task-relevant manifolds. Here task-relevant manifolds refer to the collection of activity patterns (of a certain layer) to the same task condition (e.g., the same label class). **b**, Specifically, we found that the degree of manifold untangling (quantified by manifold capacity, [Definition 2.1](#) and [Definition B.3](#)) tracks the degree of richness in feature learning. **c**, Three main contributions of this paper. More details in the corresponding section.

geometric measures, also known as Geometry Linked to Untangling Efficiency (GLUE) [Chou et al. \(2025\)](#), which provide a set of mechanistic descriptors to explain how these manifolds untangle.

To demonstrate our proposed method, we examine problems in neuroscience and machine learning and find insights that have not been reported. Our contributions are summarized below.

- ([Section 3](#)) We use manifold capacity as a representation-based method to quantify the degree of feature learning and demonstrate that it is better than conventional measures across a wide range of settings.
- ([Section 4](#)) Manifold geometry reveals previously unreported subtypes of feature learning. We find that the training of neural networks undergoes various *learning stages* as shown by the dynamics of manifold geometry, and there are diverse emergent *learning strategies* from networks having different degree of richness in learning.
- ([Section 5](#)) We find new geometric insights that have not been reported in problems from neuroscience (e.g., structural inductive biases in neural circuits) and machine learning (e.g., out-of-distribution generalization).

1.2 Related work

Feature learning has been a fundamental research problem in various domains, including neuroscience and machine learning. In neuroscience, understanding the relationship between neural

the worst-case setting. Here the manifold capacity theory is average-case in the sense of the random projection in [Definition 2.1](#) and the random up-lifting in [Definition B.3](#). This average-case nature of manifold capacity enables its connection to geometrical properties of the manifolds.

representations and task performance is a central focus (Gao and Ganguli, 2015). Representational geometry (Chung and Abbott, 2021) has emerged as a promising approach to investigate how different organizations of features can lead to better task performance (Bernardi et al., 2020; Flesch et al., 2022; Gurnani and Gajic, 2023). There were also works that attempted to infer the underlying learning rules of a neural network using representational geometry (Cao et al., 2020; Sorscher et al., 2022) and low-order statistics (Nayebi et al., 2020). In machine learning, *visualization techniques* (Zeiler and Fergus, 2014) have been widely used to gain intuitive insights into learned representations, often supplemented with specialized measures to quantify specific properties. On the theoretical front, the *kernel method* (Jacot et al., 2018; Lee et al., 2019) has been a leading approach to analytically characterize the behavior of neural networks, particularly in terms of their deviation from the corresponding kernel. This line of research includes studies on the distinction between lazy and rich regimes (Chizat et al., 2019; Geiger et al., 2020) and identifying problem settings where neural networks with feature learning outperform kernel methods (Ba et al., 2022; Dandi et al., 2023; Yang and Hu, 2021). For a more comprehensive overview of related work, see Appendix A.

A remark on terminologies. Here we clarify the terminology of *manifold untangling*, *manifold packability*, and *manifold capacity*. Manifold untangling originates from neuroscience (DiCarlo and Cox, 2007) and refers to the intuition that task-relevant manifolds become increasingly separable in a high-dimensional state space. Several methods have been proposed to quantify the degree of untangling, such as decoding accuracy (Yamins and DiCarlo, 2016; Hong et al., 2016). Manifold packability, inspired by the sphere-packing intuitions from physics and mathematics, represents an average-case notion of manifold separability. It naturally provides a more concrete framework for defining manifold untangling within a system. Finally, manifold capacity analytically quantifies manifold packability in terms of linear classification, making it a useful metric for assessing the degree of untangling. Further details on manifold capacity theory will be discussed in Section 2.2 and Appendix B.

2 Method and Setup

2.1 Rich and lazy learning in neural networks

We studied rich versus lazy learning in two standard settings: 2-layer non-linear neural networks on synthetic data and feedforward deep neural networks on real image classification datasets (Chizat et al., 2019). All analyses were performed on the test data representations in the last layer.

A scale factor for interpolating between rich and lazy regime. In all experiments, we use the *inverse scale factor* $\bar{\eta}$ as a tunable ground truth for the degree of feature learning. In particular, $\bar{\eta}$ controls the magnitude of the output of the network as in (Chizat et al., 2019). Intuitively, a larger $\bar{\eta}$ indicates that the learning rate of intermediate layers is faster compared to that of the readout weights, resulting in a richer learning process. See Appendix D and E for more details.

2-Layer non-linear neural networks. We considered standard 2-layer neural networks with non-linear activation functions and trained with gradient descent. We also considered a data model to generate random point clouds as input manifolds. This setting serves as a well-curated testbed for testing the proposed methodology and showcasing intuitions. See Appendix D for more details.

Deep neural networks. The goal of this work is to develop a framework to understand neural representations rather than pushing the benchmark. Therefore, we focused on models and settings that are large enough to see interesting phenomena, while the computational cost is still reasonable. Specifically, we considered feedforward DNN architectures such as VGG-11 (Simonyan and Zisserman, 2015) and ResNet-18 (He et al., 2016) and datasets CIFAR-10 (Krizhevsky and Hinton, 2009), CIFAR-100 (Krizhevsky and Hinton, 2009), CIFAR-10C (Hendrycks and Dietterich, 2018). This setting illustrates the applicability of our methodology to DNNs. See Appendix E for more details.

Task-relevant manifolds. Let P be the number of classes and N be the number of neurons (in the layer of interest⁴). The i -th class manifold is modeled as the convex set⁵ $\mathcal{M}_i = \text{conv}(\{\Phi(x) : x \in \mathcal{X}_i\})$ where \mathcal{X}_i is the collection of inputs in the i -th class, $\Phi(x)$ is the representation for x , and $\text{conv}(\cdot)$ denotes the convex hull of a set.

2.2 Manifold capacity theory

Manifold capacity theory (Chung et al., 2018; Chou et al., 2025) was originally developed to study the *untangling hypothesis*⁶ of invariant object recognition in vision neuroscience (DiCarlo and Cox, 2007). Manifold capacity theory (Chung et al., 2018; Chou et al., 2025) extends the classic notion of storage capacity of points (Cover, 1965; Gardner and Derrida, 1988; Gardner, 1988) to object manifolds, i.e., the collection of neural representations that are invariant to the same input category (Figure 1a, left). A *simulated* version of manifold capacity is defined as follows.

Definition 2.1 (Simulated manifold capacity (Cohen et al., 2020; Chou et al., 2025)). *Let $P, N \in \mathbb{N}$ and $\mathcal{M}_i \subseteq \mathbb{R}^N$ be convex sets for each $i \in [P] = \{1, \dots, P\}$. For each $n \in [N]$, define*

$$p_n := \Pr_{\mathbf{y}, \Pi_n} [\exists \theta \in \mathbb{R}^n : y_i \langle \theta, \mathbf{s} \rangle \geq 0, \forall i \in [P], \mathbf{s} \in \mathcal{M}_i]$$

where \mathbf{y} is a random dichotomy sampled from $\{\pm 1\}^P$ and Π_n is a random projection operator from \mathbb{R}^N to \mathbb{R}^n . Suppose $p_N = 1$, the simulated capacity of $\{\mathcal{M}_i\}_{i \in [P]}$ is defined as

$$\alpha_{sim} := \frac{P}{\sum_{n \in [N]} p_n}.$$

Intuitively, the simulated manifold capacity measures the *packability* (Chung et al., 2018) of manifolds by determining the smallest dimensional subspace needed to ensure that the manifolds can be separated. Namely, manifolds that are more packable (i.e., separable when projected to smaller dimensional subspaces) exhibit higher manifold capacity. While Definition 2.1 provides a quantitative description for *packability*, it is computationally expensive to estimate and is not analytically trackable. In (Chung et al., 2018; Chou et al., 2025), the authors resolved these issues by considering a mean-field version of the manifold capacity (formal definition deferred

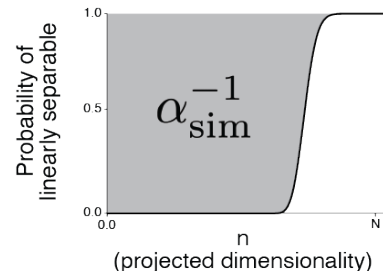


Figure 2: Simulated capacity.

⁴In this paper, we primarily consider the last layer in most experiments unless specified otherwise.

⁵In the context of linear classification, it is mathematically equivalent to study the convex hull of a manifold.

⁶In computational neuroscience, the “untangling hypothesis” posits that the brain transforms complex, entangled sensory inputs into more linearly separable representations, facilitating efficient object recognition.

to Definition B.3), denoted as α_{mf} , which is analytically trackable and has the property that $|\alpha_{\text{sim}} - \alpha_{\text{mf}}| = O(1/N)$. In particular, (Chou et al., 2025) derived that

$$\alpha_{\text{mf}}^{-1} = \frac{1}{P} \mathbb{E}_{\substack{\mathbf{y} \sim \{\pm 1\}^P \\ \mathbf{t} \sim \mathcal{N}(0, I_N)}} \left[\max_{\mathbf{s}_i \in \mathcal{M}_i} \left\{ \|\text{proj}_{\text{cone}(\{y_i \mathbf{s}_i\})} \mathbf{t}\|_2^2 \right\} \right] \quad (2.2)$$

where $\mathcal{N}(\mu, \Sigma)$ denotes the multivariate Gaussian distribution with mean μ and covariance Σ and $\text{cone}(\cdot)$ is the convex cone spanned by the vectors, i.e., $\text{cone}(\{y_i \mathbf{s}_i\}) = \{\sum_i \lambda_i y_i \mathbf{s}_i : \lambda_i \geq 0\}$.

2.3 Geometry linked to untangling efficiency (GLUE) via manifold capacity

The advantages of mean-field manifold capacity are: (i) α_{mf} can be estimated via solving a quadratic program (Algorithm 1) and (ii) Equation 2.2 connects manifold capacity to the structure of the manifolds $\{\mathcal{M}_i\}$. Specifically, for each \mathbf{y}, \mathbf{t} , define $\{\mathbf{s}_i(\mathbf{y}, \mathbf{t})\} = y_i \cdot \arg \max_{\{\mathbf{s}_i\}} \|\text{proj}_{\text{cone}(\{y_i \mathbf{s}_i\})} \mathbf{t}\|_2^2$ as the *anchor points* with respect to \mathbf{y} and \mathbf{t} . Intuitively, these anchor points are the support vectors with respect to some random projection and dichotomy as in Definition 2.1. Namely, the randomness⁷ induces a distribution of anchor points supported on the manifolds $\{\mathcal{M}_i\}$. Specifically, these anchor points are analytically linked to manifold capacity via Equation 2.2 through the capacity formula (Equation 2.2). This connection inspired the previous work (Chung et al., 2018; Chou et al., 2025) to define the following effective manifold geometric measures that capture the structure of manifolds while being analytically connected to capacity (see Figure 3c and Appendix B).

Definition 2.3 (Effective manifold geometric measures (Chou et al., 2025), simplified version). For each $i \in [P]$, define $\mathbf{s}_i^0 := \mathbb{E}_{\mathbf{y}, \mathbf{t}}[\mathbf{s}_i(\mathbf{y}, \mathbf{t})]$ as the **center** of the i -th manifold and define $\mathbf{s}_i^1(\mathbf{y}, \mathbf{t}) := \mathbf{s}_i(\mathbf{y}, \mathbf{t}) - \mathbf{s}_i^0$ to be the **axis** part of $\mathbf{s}_i(\mathbf{y}, \mathbf{t})$ for each pair of (\mathbf{y}, \mathbf{t}) .

- **Manifold dimension** captures the degree of freedom of the noises/variations within the manifolds. It is approximately $D_{\text{mf}} \approx \mathbb{E}_{\mathbf{y}, \mathbf{t}} \left[\frac{1}{P} \sum_i \left(\frac{\langle \mathbf{s}_i^1(\mathbf{y}, \mathbf{t}), \mathbf{t} \rangle}{\|\mathbf{s}_i^1(\mathbf{y}, \mathbf{t})\|_2} \right)^2 \right]$, which is analogous to the Gaussian width of the manifolds (Vershynin, 2018, Chapter 7). See Definition B.6 for the formal definition.
- **Manifold radius** captures the noise-to-signal ratio of the manifolds. It is approximately $R_{\text{mf}} \approx \mathbb{E}_{\mathbf{y}, \mathbf{t}} \left[\frac{1}{P} \sum_i \frac{\|\mathbf{s}_i^1(\mathbf{y}, \mathbf{t})\|_2^2}{\|\mathbf{s}_i^0\|_2^2} \right]$. See Definition B.6 for the formal definition.
- **Center alignment** captures the correlation between the center of different manifolds. Formally, it is defined as $\rho_{\text{mf}}^c := \frac{1}{P(P-1)} \sum_{i \neq j} |\langle \mathbf{s}_i^0, \mathbf{s}_j^0 \rangle|$.
- **Axis alignment** captures the correlation between the axis of different manifolds. Formally, it is defined as $\rho_{\text{mf}}^a := \frac{1}{P(P-1)} \sum_{i \neq j} \mathbb{E}_{\mathbf{y}, \mathbf{t}} [|\langle \mathbf{s}_i^1(\mathbf{y}, \mathbf{t}), \mathbf{s}_j^1(\mathbf{y}, \mathbf{t}) \rangle|]$.
- **Center-axis alignment** captures the correlation between the center and axis of different manifolds. Formally, it is defined as $\psi_{\text{mf}} := \frac{1}{P(P-1)} \sum_{i \neq j} \mathbb{E}_{\mathbf{y}, \mathbf{t}} [|\langle \mathbf{s}_i^0, \mathbf{s}_j^1(\mathbf{y}, \mathbf{t}) \rangle|]$.

Three important remarks on effective manifold geometric measures to be made: First, the changes in manifold capacity can be explained by the changes of these geometric measures. For example, the decrease of manifold radius and dimension makes the capacity higher (see Fig. 3c, Appendix B.4). Second, these effective geometric measures faithfully track the corresponding underlying geometric properties in well-studied mathematical settings (see Appendix B.5). Moreover, there is a simple formula connecting manifold capacity with effective geometric measure:

⁷Also known as *disorder* in spin glass theory.

$\alpha_{mf} \approx (1 + R_{mf}^{-2})/D_{mf}$ (see Appendix B for details). Finally, combining the above two points, these effective geometric measures serve as intermediate-level descriptors to investigate how different structural properties of neural manifolds contribute to the changes of task-level performance.

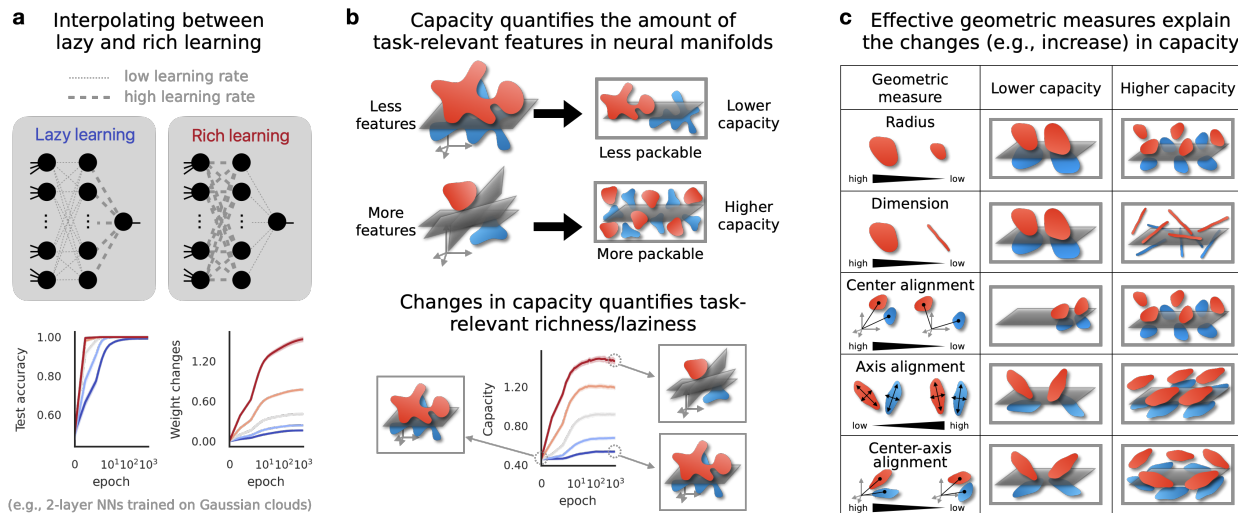


Figure 3: Our methods. **a**, Top: We adopt the method from (Chizat et al., 2019) which interpolates lazy and rich learning via adjusting a scale factor of learning rate. Bottom: Test accuracy increases during both lazy and rich training, however, the network’s weights would not change much during lazy training. **b**, Top: Higher capacity means that the neural representational space can pack more manifolds (Definition 2.1). Bottom: We propose to use changes of capacity across training to study task-relevant richness/laziness in feature learning (Section 3). Top: we consider the setting in (Chizat et al., 2019) where VGG-11 was trained on CIFAR-10. An inverse scale factor was introduced to interpolate between lazy and rich training, where smaller value (blue) corresponds to lazier learning and larger value corresponds to richer learning (red). Bottom: we show that the changes in capacity faithfully tracks the degree of richness in feature learning. **c**, Effective geometric measures drive the capacity value, providing mechanistic descriptors to study representational changes in feature learning. Center-axis alignment has a more complex relationship with capacity, discussed Section B.4.

3 Manifold capacity quantifies the degree of feature learning

In this section, we provide both empirical and theoretical justifications for using the increase in capacity during training as a measure to quantify the degree of richness (or the amount of task-relevant features) in feature learning. Furthermore, we compare our method with conventional approaches in the study of lazy versus rich learning, highlighting the new insights uncovered by our approach.

3.1 Justifications of capacity for quantifying the lazy versus rich dichotomy

Empirical justification in standard settings. We start with empirically justifying the use of capacity to quantify the degree of feature learning. A classic result in the literature of lazy versus rich training is to train a lazy network where the test accuracy improves, but the weight matrices (or kernels) do not change much before and after training. We consider two settings in (Chizat

et al., 2019), one is feedforward DNNs (VGG-11 and ResNet-18) trained on CIFAR-10 (Figure 3b), and the other is 2-layer non-linear NNs trained on random point clouds (Figure 4a). In both cases, we observe that the manifolds are more untangled when training is richer and capacity correctly tracks the degree of feature learning (the ground truth being the scale parameter $\bar{\eta}$). This provides empirical justification for the use of capacity as well as evidence for manifold untangling in the rich learning regime.

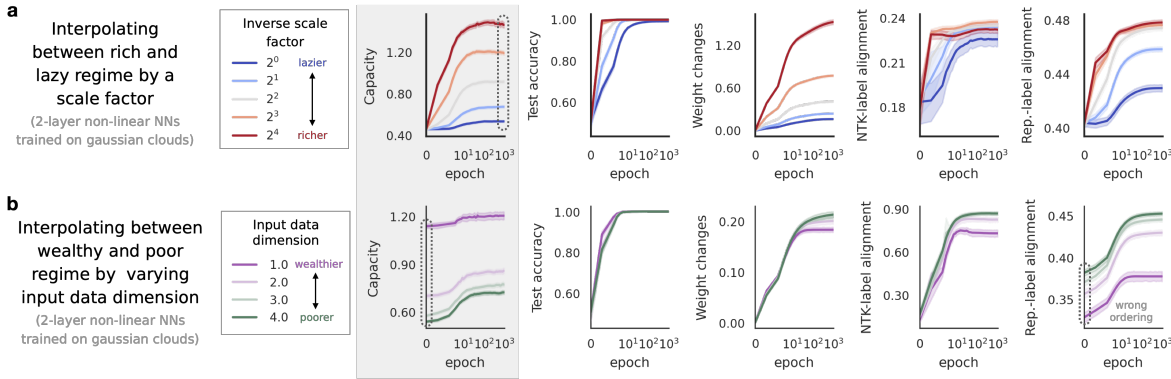


Figure 4: Capacity as a measure for the degree of feature learning. See Section D.1 for the experimental setup. **a**, We interpolated between lazy and rich regime in 2-layer NNs trained to classify Gaussian clouds. We found that capacity could tell the difference between the underlying scale parameter better than the other conventional methods. **b**, We fixed a scale parameter and initialized the input Gaussian clouds with different dimensions (the higher the poorer the initial representations are for each class). We found that capacity could tell the difference in the amount of tasks-relevant features at initialization than other conventional methods. Specifically, the representation-label alignment would characterize the wrong ordering of wealthiness in initial features.

Theoretical justification on 2-layer non-linear neural networks. To strengthen the connection between capacity and feature learning, we next consider a well-studied theoretical model (Ba et al., 2022; Montanari et al., 2019) and analytically characterize the relationship between capacity, prediction error, and the effective degree of richness. Concretely, we consider the training of a fully-connected 2-layer network of the form $f(\mathbf{x}) = \frac{1}{\sqrt{N}} \mathbf{a}^\top \sigma(W^\top \mathbf{x})$, where $\mathbf{x} \in \mathbb{R}^d$ is an input, $W \in \mathbb{R}^{N \times d}$ is the hidden layer matrix, $\mathbf{a} \in \mathbb{R}^N$ is the readout weight, and $\sigma : \mathbb{R} \rightarrow \mathbb{R}$ is the (non-linear) activation function. To study feature learning in this setting, it is common to consider W to be randomly initialized (i.e., random feature model (Rahimi and Recht, 2007)) and update via gradient descent with squared loss. Meanwhile, the readout weight \mathbf{a} is randomly initialized and fixed to avoid lazy learning (where the network minimally adjusts the hidden layer and focuses on learning a good readout weight) as well as enable mathematical analysis (Ba et al., 2022). Input data and label $(\mathbf{x}_1, y_1), \dots, (\mathbf{x}_{P_{\text{train}}}, y_{P_{\text{train}}})$ were randomly generated by a teacher-student setting, where there is a hidden signal direction β^* that correlates with the label (see Setting C.2 for the full setting). As previously proved in (Ba et al., 2022) (see Proposition C.5), in the proportional asymptotic limit (i.e., $P_{\text{train}}, d, N \rightarrow \infty$ at the same rate), the first-step gradient update can be approximated by a rank-1 matrix that contains label information, resulting in the updated weight to be more aligned with the hidden signal β^* . Hence, in this setting, the learning rate η can be used as the ground-truth to measure the amount of task-relevant information (i.e., richness in learning)

in the model representation after gradient updates.

We extend the previous results in (Ba et al., 2022) from a regression setting to a classification setting. Specifically, We prove that capacity correctly tracks the effective degree of richness after one gradient step⁸. Moreover, we derive a monotone connection between capacity and prediction accuracy. Here, we provide an informal statement of our results and leave the formal version and proof in Appendix C.

Theorem 3.1. *Given Assumption C.1 and Setting C.2. Let $0 < \eta < \infty$ be the learning rate of a one-step gradient descent with squared loss and $\psi_1 = \frac{N}{d}, \psi_2 = \frac{P_{\text{train}}}{d}$ where P_{train} is the number of training points, d is the input dimension, and N is the number of hidden neurons. Let $\alpha_{P_{\text{train}},d,N}(\eta)$ be the capacity and let $\text{Acc}_{P_{\text{train}},d,N}(\eta)$ be the prediction accuracy after a gradient step with learning rate η . We have*

1. *(Capacity tracks the degree of richness) $\alpha_{P_{\text{train}},d,N}(\eta) \xrightarrow{P_{\text{train}},d,N \rightarrow \infty} \alpha(\eta, \psi_1, \psi_2)$ where $\alpha(\cdot, \cdot, \cdot)$ is defined in Theorem C.4. Specifically, $\alpha(\eta, \psi_1, \psi_2) < \alpha(\eta', \psi_1, \psi_2)$ for every $0 < \eta < \eta'$.*
2. *(Capacity links to prediction accuracy) $\text{Acc}_{P_{\text{train}},d,N}(\eta) \xrightarrow{P_{\text{train}},d,N \rightarrow \infty} \text{Acc}(\eta, \psi_1, \psi_2)$ where $\text{Acc}(\eta, \psi_1, \psi_2)$ is formally defined in Theorem C.4. In particular, there exists an increasing and invertible function $h_{\psi_1, \psi_2} : \mathbb{R}_+ \rightarrow [0, 1]$ such that $\text{Acc}(\eta, \psi_1, \psi_2) = h_{\psi_1, \psi_2}(\alpha(\eta, \psi_1, \psi_2))$.*

The above theorem justifies the usage of capacity as a measure for the degree of richness in feature learning within a well-studied theoretical setting. We remark that our proof requires substantial technical improvements from (Ba et al., 2022) due to the difference between regression and classification (e.g., analyzing the margin of the Gaussian equivalent model after one-step gradient using tools from (Montanari et al., 2019), Proposition C.7).

3.2 Comparison with conventional feature learning measures.

Here we compare the capacity with several common measures for feature learning: accuracy curves, weight changes, and alignment methods. Concretely, weight changes at the t -th epoch is defined as $\|W_t - W_0\|_F / \|W_0\|_F$ where W_t is the weight matrix at the t -th epoch. NTK-label alignment and representation-label alignment at the t -th epoch are defined as $\text{CKA}(K_t^{\text{NTK}}, \mathbf{y}\mathbf{y}^\top)$ and $\text{CKA}(X_t X_t^\top, \mathbf{y}\mathbf{y}^\top)$ respectively, where \mathbf{y} is the label vector, $\text{CKA}(\cdot, \cdot)$ is the center kernel alignment measure (Kornblith et al., 2019), K_t^{NTK} is the neural tangent kernel and X_t is the representational matrix at the t -th epoch. In order to test these measures in a wide variety of settings, we consider 2-layer NNs with synthetic data where we can vary a wide range of parameters. See Appendix A for a detailed introduction to these methods and Appendix D for more experimental details.

Capacity can detect the presence of task-relevant features in data. In Figure 4a, we consider 2-layer NNs trained on random Gaussian clouds with gradient descent. We vary the scale parameter of the network to interpolate between lazy and rich regimes as done in (Chizat et al., 2019). We find that capacity is better at telling the difference of effective richness (i.e., the scale parameter) of the training than other conventional measures (Figure 4a). In particular, when the training is richer, we expect the representations to exhibit more complex structures. Manifold capacity excels at extracting task-relevant structures in representations because it is data-driven and free from additional statistical assumptions on the data (Chung et al., 2018; Chou et al., 2025).

⁸Here we follow the convention in (Ba et al., 2022) and study only the first gradient step as the key Gaussian equivalence step might not hold for more steps as remarked in footnote 2 of (Ba et al., 2022).

Capacity can quantify the differences in task-relevant features at initialization. When comparing two networks with different initializations, focusing solely on network changes can overlook differences in features present at initialization. Here, we use the capacity value at initialization to determine whether a network is in a wealthy regime (i.e., possessing more task-relevant features) or a poor regime (i.e., possessing less task-relevant features), as shown in (Figure 4b). The wealthy versus poor distinction provides insight into the network’s initial state, allowing for a more comprehensive comparison of different settings (see ‘Section 5.1 for an example).

	Our approach (manifold geometry)	Accuracy	Weight changes	NTK-label alignment	Representation-label alignment
Detect the changes in features	✓	✗	✓	✓	✓
Quantify the amount of task-relevant features	✓	✗	✗	✗ ⁹	✗ ⁹
Representation-based	✓	✗	✗	✗	✓
Delineate subtypes of feature learning	✓	✗	✗	✗	✗

Table 1: Comparison with conventional measures used in lazy versus rich learning.

4 Manifold Geometry Reveals Subtypes of Feature Learning

In this section, we demonstrate that feature learning is much richer than the lazy versus rich dichotomy. In particular, we use manifold geometric measures (Figure 3c, and Appendix B for details) to delineate the differences in the learned features (learning strategies) of neural networks and representational changes throughout training (learning stages). The key takeaway from this section is the ability of our method to reveal task-relevant changes in neural representations.

4.1 Geometric differences in learned features: Learning strategies

To increase capacity, a network can shrink the radius or compress the dimension of neural manifolds (Figure 3c). We demonstrate in 2-layer NNs the emergence of distinct learning strategies driven by different factors. In Figure 5a, we consider the setting in Figure 4a where we interpolate the degree of richness in feature learning via an inverse scale factor. As training moves from the lazy to a richer regime (blue to gray), the network compresses both the radius and dimension to increase capacity. Interestingly, in an even richer regime (gray to red), the network sacrifices radius to further reduce dimension. In Figure 5b, we consider the setting in Figure 4b where we interpolate the wealth of initialization by varying input data dimension. For the wealthiest initialization (purple), the network primarily compresses radius. For poorer initialization (green), both radius and dimension are compressed in lazier training, while in the richer regime (e.g., inverse scale factor 2⁴), the network sacrifices radius for further dimension compression. In summary, varying degrees of richness in feature learning can exhibit different learning mechanisms, as captured by manifold geometry.

4.2 Manifold geometry changes through the course of training: Learning stages

Neural networks learn in a highly non-monotonic manner throughout the training period. Examples include double descent (Belkin et al., 2019; Nakkiran et al., 2021; Mei and Montanari, 2022) and

⁹See Figure 4 for examples of how NTK-label alignment and representation-label alignment could fail at quantifying the amount task-relevant features.

grokking (Power et al., 2022; Liu et al., 2022; Nanda et al., 2023; Kumar et al., 2024). Previous works have analytically or empirically described the different stages/phases such as comprehension, grokking, memorization, and confusion (Liu et al., 2022) through the trajectory of accuracy curves.

From Figure 5a,b we observe distinct stages of manifold geometry evolution during training in 2-layer networks. In the very rich regime, the network initially compresses both radius and dimension, then increases radius to further reduce dimension. In Figure 5c, we examine a standard setting where VGG-11 is trained on CIFAR-10. Despite the rapid saturation of training and test accuracy, at least four stages of geometric changes are evident (see Figure 3c for analytical connections between geometric measures and capacity): a *clustering stage* (initial manifold compression), followed by a *structuring stage* (increasing alignment), a *separating stage* (decreasing alignment to push manifolds apart), and a final *stabilizing stage* (further reducing center alignment).

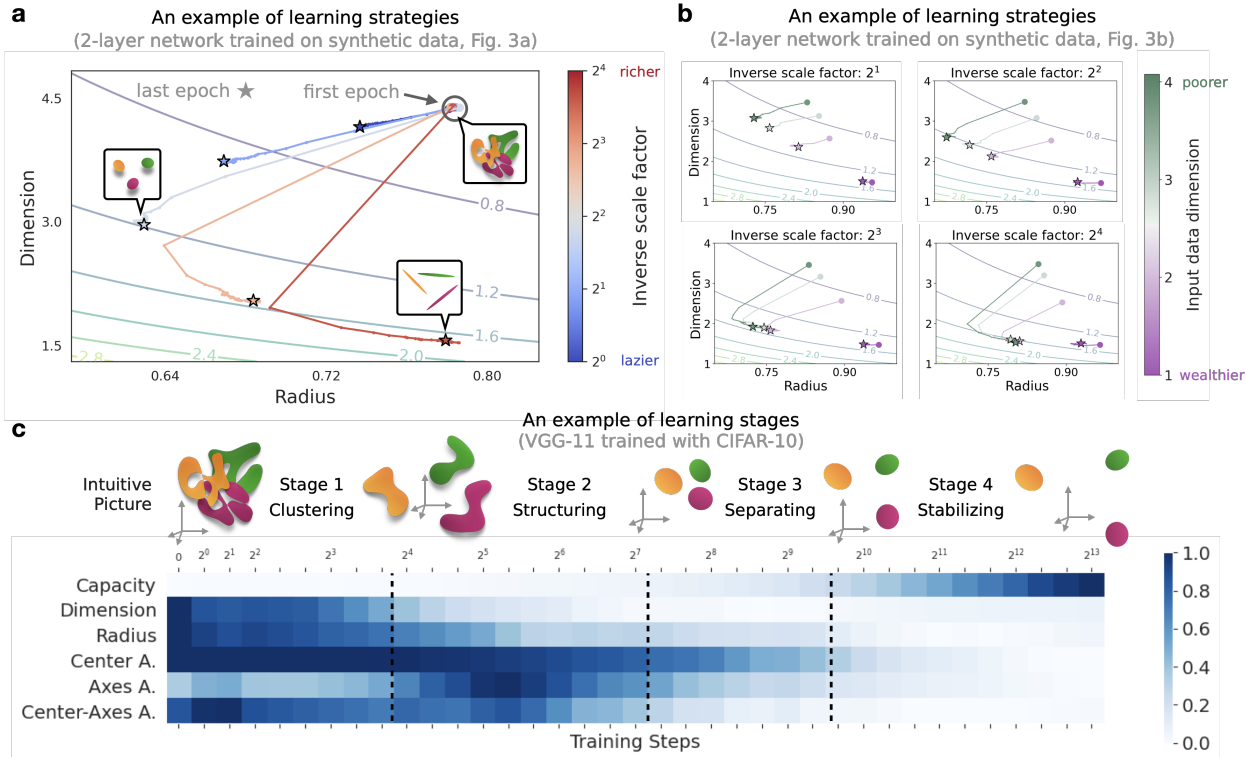


Figure 5: Manifold geometry characterizes learning strategies and learning stages. **a**, Capacity contour plot of the example from Figure 4a. The x-axis is the average manifold radius R_{mf} , the y-axis is the average manifold dimension D_{mf} , and the contour is the geometric approximation of capacity, i.e., $\alpha_{mf} \approx (1 + R_{mf}^{-2})/D_{mf}$ (see Appendix B for details). **b**, Capacity contour plot of the example from Figure 4b. **c**, Normalized manifold geometry dynamics plot of VGG-11 trained with CIFAR-10. The values in each row are rescaled so that the max value is 1 and the min value is 0.

5 Applications to Neuroscience and Machine Learning Problems

In previous sections, we used capacity to quantify the degree of feature learning and delineate the learning stages and strategies through effective geometry. In this section, we apply our framework to find geometric insights in problems from neuroscience and machine learning.

5.1 Structural inductive biases in neural circuits

We study recurrent neural networks (RNNs) that are trained on standard neuroscience tasks such as perceptual decision making (Britten et al., 1992) (Figure 6a). We adopt the setting from previous work (Liu et al., 2024) on investigating how differences in connectivity initialization affect the learning process. In particular, previous work used the weight changes of RNNs before and after training as a measure to quantify if a network is in rich or lazy training regimes (Figure 6b). Here, we use our methods of capacity and its effective geometry to study such structural biases of neural circuits in a data-driven way (i.e., from neural activity patterns instead of weight matrix).

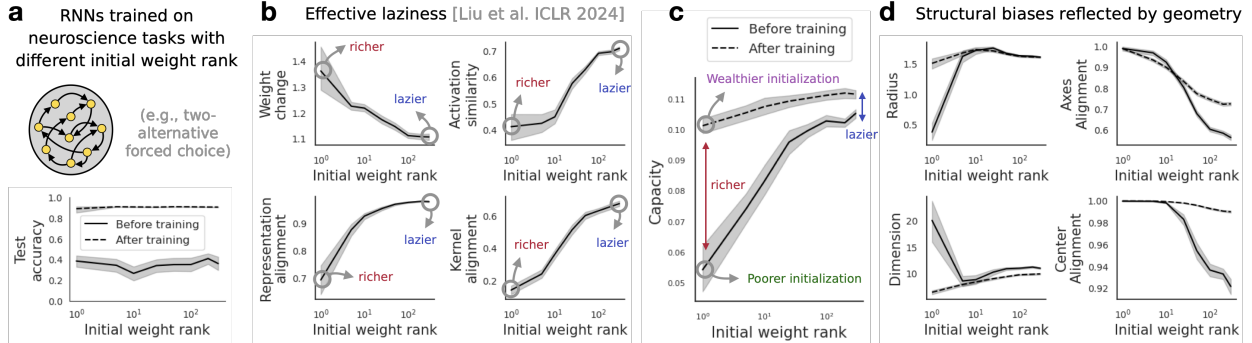


Figure 6: Structural inductive biases in neural circuits. **a**, We consider RNNs trained on standard neuroscience tasks. **b**, Previous work (Liu et al., 2024) found that the initial weight rank of the recurrent connectivity matrix leads to an inductive bias toward effectively richer or lazier training. **c**, We find that RNNs trained with different initial weight rank reach the same capacity value at final epoch. It is the difference in capacity at initialization that makes RNNs with small initial weight rank richer in training. **d**, Despite having the same capacity at final epoch, RNNs with different initial weight rank exhibit different manifold geometry.

Experimental setup. We use the neurogym package (Molano-Mazon et al., 2022) to simulate common cognitive tasks, including perceptual decision making, delayed matching, etc. To study how connectivity structure impacts learning strategies, we initialize recurrent neural networks (RNN) weights with varying ranks (low-rank weight has lower connectivity and higher initial bias and vice versa) via Singular Value Decomposition (similar setup used in (Liu et al., 2024)). The RNN have 300 hidden units, 1 layer, with ReLU activations, and are trained for 10000 iterations using SGD optimizer. (more details can be found in the Appendix section F). Manifold capacity and effective geometric measures are computed using representations from the hidden states.

Our findings. First, we study the training dynamics of capacity value in RNNs with various initial weight rank (Figure 6c). In agreement with the previous finding in (Liu et al., 2024) using weight changes, we find that the capacity changes of the small initial weight rank RNNs are higher than those of the large initial weight rank RNNs. Interestingly, the capacity values at the final epoch are about the same for RNNs with different initial weight rank. It is the difference in capacity value at initialization that distinguishes the learning dynamics of RNNs with different initial weight rank. Namely, small initial weight rank RNNs are in the poorer-richer feature learning regime, while large initial weight rank RNNs are in the wealthier-lazier feature learning (Figure 6c).

Next, although the capacity values of RNNs at the final epoch are about the same for different initial weight ranks, we find that their geometric organizations are quite different (Figure 6d). For

example, poorer-richer learning (i.e., small initial weight rank) ends up with a larger radius but smaller dimension, while it is the opposite for wealthier-lazier learning (i.e., large initial weight rank). This finding suggests that there are structural biases in RNNs at the manifold geometry level.

Takeaways. Conventional methods for studying rich versus lazy learning may only quantify the relative improvement of task-relevant features and overlook the potential difference due to the absolute encoding capacity of different initialization configurations (e.g, low-rank vs high-rank initialization). Our method of using manifold capacity and GLUE is able to overcome this limitation and provide a wide range of geometric signatures to investigate the structural inductive biases of learning in neural circuits.

5.2 Out-of-distribution generalization

Out-of-distribution (OOD) generalization refers to the scenario when the training distribution $(\mathbf{x}, y) \sim \mathcal{D}_{\text{train}}$ is different from the test distribution $(\mathbf{x}, y) \sim \mathcal{D}_{\text{test}}$. Here we focus on the case where the label set in $\mathcal{D}_{\text{test}}$ is different from that in $\mathcal{D}_{\text{train}}$.

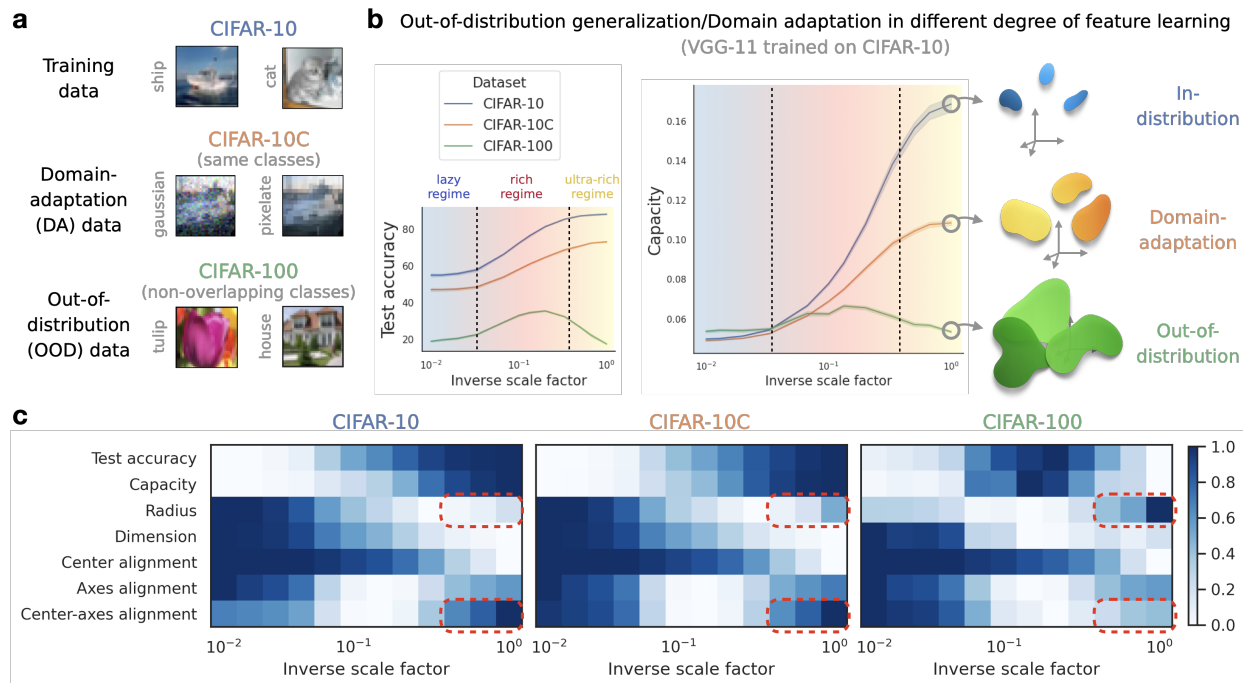


Figure 7: Out of distribution generalization. **a**, CIFAR-10c as a domain adaptation (DA) dataset and CIFAR-100 as an OOD dataset. **b**, Test accuracy improves for CIFAR-10 and CIFAR-10C as the training becomes richer and richer while the linear probe accuracy for CIFAR-100 would drastically drop in the ultra-rich training regime. **c**, Effective manifold geometry of CIFAR-100 reveals that the expansion of manifold radius and the increase of center-axis alignment explain the failure of OOD generalization in the ultra-rich regime. The color is normalized for each row respectively.

Experimental setup. For each model pre-trained on CIFAR-10, we train a linear classifier (i.e., linear probe (Alain and Bengio, 2016)) on top of the last-layer representation with CIFAR-100 train set, and then evaluate the linear probe’s performance on CIFAR-100 test set (see more details in Appendix E.4). We also consider a corrupted version of CIFAR-10, the CIFAR-10C dataset (Hendrycks and Dietterich, 2018) as an example of domain adaptation (DA) task. Finally, we compute the manifold capacity and effective geometric measures on these last-layer representations.

Our findings. We see that the test accuracy of the OOD dataset increases when the network enters the rich learning regime ($\bar{\eta}$ around 0.1) but decreases drastically when the degree of feature learning is too rich ($\bar{\eta}$ around 1.0). The failure in such *ultra-rich* feature learning regime is different from the test accuracy of both CIFAR-10 and CIFAR-10C (Figure 7b). Looking at the capacity and effective geometry (Figure 7c), we first see strong correlations between the capacity and test accuracy, which warrants the use of effective geometry. Next, we find that the expansion of manifold radius and the increase of center-axis alignment in the ultra-rich regime explain the drop of capacity. Interestingly, we also see an architectural difference where it is the increment in dimension in the ultra-rich regime explaining the drop of capacity in ResNet-18 (Figure 17).

Takeaways. Our method of using manifold capacity and GLUE is able to identify correlations between the geometric signatures of the in-distribution manifolds and that of the OOD manifolds. This may lead to potential applications in mitigating the failure of OOD generalization by merely inspecting the training data. We leave it as an interesting future direction to extend our study, applying these geometric insights to improve OOD generalization performance.

6 Conclusion and Discussion

Feature learning serves as a crucial *feature* in the study of neural networks in both computational neuroscience and machine learning, and it is much *richer* than the lazy versus rich dichotomy. Understanding the connection between feature learning and performance further promises the future design of network architectures and learning algorithms with enhanced reliability and the requisite model transparency for practical applications.

The primary contribution of this work is to demonstrate how the perspective of task-relevant manifold untangling (quantified by manifold capacity and delineated by manifold geometric measures) can enhance our understanding of feature learning at an intermediate level. We propose several promising future directions, including extending the theoretical analysis to more realistic settings, exploring applications in other types of DNN (e.g., recurrent networks, transformers) and addressing relevant scientific inquiries in neuroscience, such as inferring plasticity mechanisms from observed learning dynamics in neural data, and predicting learning-induced changes across brain regions. We believe that investigations in these intermediate-level understandings can be leveraged to design more robust, generalizable, and safer deep neural networks, as well as more accurate models for neuroscience applications.

Acknowledgements

We thank the members of Chung lab for the discussion regarding many preliminary results and early versions of the manuscript. This work was supported by the Center for Computational Neuroscience at the Flatiron Institute, Simons Foundation, and by NIH grant R01DA059220. S.C. was partially supported by a Sloan Research Fellowship, a Klingenstein-Simons Award, and the Samsung Advanced Institute of Technology project, “Next Generation Deep Learning: From Pattern

Recognition to AI.” All experiments were performed using the Flatiron Institute’s high-performance computing cluster.

Code Availability

Codes will be available for public usage in the final version. Requests on accessing to the current version of the code should be made to the first and corresponding author.

References

- Alain, G. and Bengio, Y. (2016). Understanding intermediate layers using linear classifier probes. *arXiv preprint arXiv:1610.01644*.
- Allen-Zhu, Z., Li, Y., and Liang, Y. (2019). Learning and generalization in overparameterized neural networks, going beyond two layers. *Advances in neural information processing systems*, 32.
- Amit, D. J., Gutfreund, H., and Sompolinsky, H. (1987). Statistical mechanics of neural networks near saturation. *Annals of physics*, 173(1):30–67.
- Ansuini, A., Laio, A., Macke, J. H., and Zoccolan, D. (2019). Intrinsic dimension of data representations in deep neural networks. *Advances in Neural Information Processing Systems*, 32.
- Arora, S., Du, S., Hu, W., Li, Z., and Wang, R. (2019). Fine-grained analysis of optimization and generalization for overparameterized two-layer neural networks. In *International Conference on Machine Learning*, pages 322–332. PMLR.
- Ba, J., Erdogdu, M. A., Suzuki, T., Wang, Z., Wu, D., and Yang, G. (2022). High-dimensional asymptotics of feature learning: How one gradient step improves the representation. *Advances in Neural Information Processing Systems*, 35:37932–37946.
- Bahri, Y., Dyer, E., Kaplan, J., Lee, J., and Sharma, U. (2021). Explaining neural scaling laws. *arXiv preprint arXiv:2102.06701*.
- Belinkov, Y., Durrani, N., Dalvi, F., Sajjad, H., and Glass, J. (2017). What do neural machine translation models learn about morphology? In Barzilay, R. and Kan, M.-Y., editors, *Proceedings of the 55th Annual Meeting of the Association for Computational Linguistics (Volume 1: Long Papers)*, pages 861–872, Vancouver, Canada. Association for Computational Linguistics.
- Belkin, M., Hsu, D., Ma, S., and Mandal, S. (2019). Reconciling modern machine-learning practice and the classical bias–variance trade-off. *Proceedings of the National Academy of Sciences*, 116(32):15849–15854.
- Bernardi, S., Benna, M. K., Rigotti, M., Munuera, J., Fusi, S., and Salzman, C. D. (2020). The geometry of abstraction in the hippocampus and prefrontal cortex. *Cell*, 183(4):954–967.
- Bordelon, B., Canatar, A., and Pehlevan, C. (2020). Spectrum dependent learning curves in kernel regression and wide neural networks. In *International Conference on Machine Learning*, pages 1024–1034. PMLR.
- Bordelon, B. and Pehlevan, C. (2022). The influence of learning rule on representation dynamics in wide neural networks. In *The Eleventh International Conference on Learning Representations*.

- Britten, K., Shadlen, M., Newsome, W., and Movshon, J. (1992). The analysis of visual motion: a comparison of neuronal and psychophysical performance. *Journal of Neuroscience*.
- Canatar, A., Bordelon, B., and Pehlevan, C. (2021). Spectral bias and task-model alignment explain generalization in kernel regression and infinitely wide neural networks. *Nature communications*, 12(1):2914.
- Cao, Y., Summerfield, C., and Saxe, A. (2020). Characterizing emergent representations in a space of candidate learning rules for deep networks. *Advances in Neural Information Processing Systems*, 33:8660–8670.
- Chizat, L., Oyallon, E., and Bach, F. (2019). On lazy training in differentiable programming. *Advances in neural information processing systems*, 32.
- Chou, C.-N., Kim, R., Arend, L., Yang, Y.-Y., Mensh, B., Slatton, W., Wakhloo, A. J., Shim, W. M., Perich, M., and Chung, S. (2025). Geometry linked to untangling efficiency reveals structure and computation in neural populations. *bioRxiv*.
- Chung, S. and Abbott, L. F. (2021). Neural population geometry: An approach for understanding biological and artificial neural networks. *Current opinion in neurobiology*, 70:137–144.
- Chung, S., Lee, D. D., and Sompolinsky, H. (2018). Classification and geometry of general perceptual manifolds. *Physical Review X*.
- Cohen, U., Chung, S., Lee, D. D., and Sompolinsky, H. (2020). Separability and geometry of object manifolds in deep neural networks. *Nature communications*.
- Cover, T. M. (1965). Geometrical and statistical properties of systems of linear inequalities with applications in pattern recognition. *IEEE transactions on electronic computers*, pages 326–334.
- Damian, A., Lee, J., and Soltanolkotabi, M. (2022). Neural networks can learn representations with gradient descent. In *Conference on Learning Theory*, pages 5413–5452. PMLR.
- Dandi, Y., Krzakala, F., Loureiro, B., Pesce, L., and Stephan, L. (2023). How two-layer neural networks learn, one (giant) step at a time. In *NeurIPS 2023 Workshop on Mathematics of Modern Machine Learning*.
- DiCarlo, J. J. and Cox, D. D. (2007). Untangling invariant object recognition. *Trends in cognitive sciences*, 11(8):333–341.
- Du, S., Lee, J., Li, H., Wang, L., and Zhai, X. (2019). Gradient descent finds global minima of deep neural networks. In *International conference on machine learning*, pages 1675–1685. PMLR.
- Du, S. S., Zhai, X., Póczos, B., and Singh, A. (2018). Gradient descent provably optimizes over-parameterized neural networks. *arXiv preprint arXiv:1810.02054*.
- Ehrlich, D. B., Stone, J. T., Brandfonbrener, D., Atanasov, A., and Murray, J. D. (2021). Psychrnn: An accessible and flexible python package for training recurrent neural network models on cognitive tasks. *eneuro*, 8(1).
- Engstrom, L., Ilyas, A., Santurkar, S., Tsipras, D., Tran, B., and Madry, A. (2019). Adversarial robustness as a prior for learned representations. *arXiv preprint arXiv:1906.00945*.

- Erhan, D., Bengio, Y., Courville, A., and Vincent, P. (2009). Visualizing higher-layer features of a deep network. *Technical Report, Univeristé de Montréal*.
- Flesch, T., Juechems, K., Dumbalska, T., Saxe, A., and Summerfield, C. (2022). Orthogonal representations for robust context-dependent task performance in brains and neural networks. *Neuron*, 110(7):1258–1270.
- Gao, P. and Ganguli, S. (2015). On simplicity and complexity in the brave new world of large-scale neuroscience. *Current opinion in neurobiology*, 32:148–155.
- Gardner, E. (1988). The space of interactions in neural network models. *Journal of physics A: Mathematical and general*, 21(1):257.
- Gardner, E. and Derrida, B. (1988). Optimal storage properties of neural network models. *Journal of Physics A: Mathematical and general*, 21(1):271.
- Geiger, M., Spigler, S., Jacot, A., and Wyart, M. (2020). Disentangling feature and lazy training in deep neural networks. *Journal of Statistical Mechanics: Theory and Experiment*, 2020(11):113301.
- Ghosh, A., Mondal, A. K., Agrawal, K. K., and Richards, B. (2022). Investigating power laws in deep representation learning. *arXiv preprint arXiv:2202.05808*.
- Girshick, R., Donahue, J., Darrell, T., and Malik, J. (2014). Rich feature hierarchies for accurate object detection and semantic segmentation. In *Proceedings of the IEEE conference on computer vision and pattern recognition*, pages 580–587.
- Glorot, X. and Bengio, Y. (2010). Understanding the difficulty of training deep feedforward neural networks. In *Proceedings of the thirteenth international conference on artificial intelligence and statistics*, pages 249–256. JMLR Workshop and Conference Proceedings.
- Gurnani, H. and Gajic, N. A. C. (2023). Signatures of task learning in neural representations. *Current opinion in neurobiology*, 83:102759.
- He, K., Zhang, X., Ren, S., and Sun, J. (2016). Deep residual learning for image recognition. In *Proceedings of the IEEE conference on computer vision and pattern recognition*, pages 770–778.
- Hendrycks, D. and Dietterich, T. (2018). Benchmarking neural network robustness to common corruptions and perturbations. In *International Conference on Learning Representations*.
- Hofmann, T., Schölkopf, B., and Smola, A. J. (2008). Kernel methods in machine learning. *The Annals of Statistics*, 36(3):1171–1220.
- Hong, H., Yamins, D. L., Majaj, N. J., and DiCarlo, J. J. (2016). Explicit information for category-orthogonal object properties increases along the ventral stream. *Nature neuroscience*, 19(4):613–622.
- Hopfield, J. J. (1982). Neural networks and physical systems with emergent collective computational abilities. *Proceedings of the national academy of sciences*, 79(8):2554–2558.
- Jacot, A., Gabriel, F., and Hongler, C. (2018). Neural tangent kernel: Convergence and generalization in neural networks. *Advances in neural information processing systems*, 31.

- Jacot, A., Gabriel, F., and Hongler, C. (2020). Neural tangent kernel: Convergence and generalization in neural networks.
- Karp, S., Winston, E., Li, Y., and Singh, A. (2021). Local signal adaptivity: Provable feature learning in neural networks beyond kernels. *Advances in Neural Information Processing Systems*, 34:24883–24897.
- Kirkpatrick, J., Pascanu, R., Rabinowitz, N., Veness, J., Desjardins, G., Rusu, A. A., Milan, K., Quan, J., Ramalho, T., Grabska-Barwinska, A., et al. (2017). Overcoming catastrophic forgetting in neural networks. *Proceedings of the national academy of sciences*, 114(13):3521–3526.
- Kirsanov, A., Chou, C.-N., Cho, K., and Chung, S. (2025). The geometry of prompting: Unveiling distinct mechanisms of task adaptation in language models. In *The 2025 Annual Conference of the Nations of the Americas Chapter of the ACL (NAACL 2025)*.
- Kornblith, S., Norouzi, M., Lee, H., and Hinton, G. (2019). Similarity of neural network representations revisited.
- Kriegeskorte, N. and Kievit, R. A. (2013). Representational geometry: integrating cognition, computation, and the brain. *Trends in cognitive sciences*, 17(8):401–412.
- Krizhevsky, A. and Hinton, G. (2009). Learning multiple layers of features from tiny images. Technical report, University of Toronto, Toronto, Ontario.
- Krizhevsky, A., Sutskever, I., and Hinton, G. E. (2012). Imagenet classification with deep convolutional neural networks. *Advances in neural information processing systems*, 25.
- Kumar, T., Bordelon, B., Gershman, S. J., and Pehlevan, C. (2024). Grokking as the transition from lazy to rich training dynamics. In *The Twelfth International Conference on Learning Representations*.
- LeCun, Y., Bottou, L., Bengio, Y., and Haffner, P. (1998). Gradient-based learning applied to document recognition. *Proceedings of the IEEE*, 86(11):2278–2324.
- Lee, J., Xiao, L., Schoenholz, S., Bahri, Y., Novak, R., Sohl-Dickstein, J., and Pennington, J. (2019). Wide neural networks of any depth evolve as linear models under gradient descent. *Advances in neural information processing systems*, 32.
- Liu, Y. H., Baratin, A., Cornford, J., Mihalas, S., SheaBrown, E. T., and Lajoie, G. (2024). How connectivity structure shapes rich and lazy learning in neural circuits. In *The Twelfth International Conference on Learning Representations*.
- Liu, Z., Kitouni, O., Nolte, N. S., Michaud, E., Tegmark, M., and Williams, M. (2022). Towards understanding grokking: An effective theory of representation learning. *Advances in Neural Information Processing Systems*, 35:34651–34663.
- Mante, V., Sussillo, D., Shenoy, K. V., and Newsome, W. T. (2013). Context-dependent computation by recurrent dynamics in prefrontal cortex. *Nature*, 503(7474):78–84.
- Mei, S. and Montanari, A. (2022). The generalization error of random features regression: Precise asymptotics and the double descent curve. *Communications on Pure and Applied Mathematics*, 75(4):667–766.

- Miller, E. K., Erickson, C. A., and Desimone, R. (1996). Neural mechanisms of visual working memory in prefrontal cortex of the macaque. *Journal of neuroscience*, 16(16):5154–5167.
- Molano-Mazon, M., Barbosa, J., Pastor-Ciurana, J., Fradera, M., ZHANG, R.-Y., Forest, J., del Pozo Lerida, J., Ji-An, L., Cueva, C. J., de la Rocha, J., and et al. (2022). Neurogym: An open resource for developing and sharing neuroscience tasks.
- Montanari, A., Ruan, F., Sohn, Y., and Yan, J. (2019). The generalization error of max-margin linear classifiers: High-dimensional asymptotics in the overparametrized regime. *arXiv e-prints*, pages arXiv–1911.
- Nakkiran, P., Kaplun, G., Bansal, Y., Yang, T., Barak, B., and Sutskever, I. (2021). Deep double descent: Where bigger models and more data hurt. *Journal of Statistical Mechanics: Theory and Experiment*, 2021(12):124003.
- Nanda, N., Chan, L., Lieberum, T., Smith, J., and Steinhardt, J. (2023). Progress measures for grokking via mechanistic interpretability. *arXiv preprint arXiv:2301.05217*.
- Nayebi, A., Srivastava, S., Ganguli, S., and Yamins, D. L. (2020). Identifying learning rules from neural network observables. *Advances in Neural Information Processing Systems*, 33:2639–2650.
- Niv, Y. (2019). Learning task-state representations. *Nature neuroscience*, 22(10):1544–1553.
- Olah, C., Mordvintsev, A., and Schubert, L. (2017). Feature visualization. *Distill*. <https://distill.pub/2017/feature-visualization>.
- Olshausen, B. A. and Field, D. J. (1996). Emergence of simple-cell receptive field properties by learning a sparse code for natural images. *Nature*, 381(6583):607–609.
- Paraouty, N., Yao, J. D., Varnet, L., Chou, C.-N., Chung, S., and Sanes, D. H. (2023). Sensory cortex plasticity supports auditory social learning. *Nature communications*, 14(1):5828.
- Poort, J., Khan, A. G., Pachitariu, M., Nemri, A., Orsolic, I., Krupic, J., Bauza, M., Sahani, M., Keller, G. B., Mrsic-Flogel, T. D., et al. (2015). Learning enhances sensory and multiple non-sensory representations in primary visual cortex. *Neuron*, 86(6):1478–1490.
- Power, A., Burda, Y., Edwards, H., Babuschkin, I., and Misra, V. (2022). Grokking: Generalization beyond overfitting on small algorithmic datasets. *arXiv preprint arXiv:2201.02177*.
- Raghu, M., Unterthiner, T., Kornblith, S., Zhang, C., and Dosovitskiy, A. (2021). Do vision transformers see like convolutional neural networks? In Ranzato, M., Beygelzimer, A., Dauphin, Y., Liang, P., and Vaughan, J. W., editors, *Advances in Neural Information Processing Systems*, volume 34, pages 12116–12128. Curran Associates, Inc.
- Rahaman, N., Baratin, A., Arpit, D., Draxler, F., Lin, M., Hamprecht, F., Bengio, Y., and Courville, A. (2019). On the spectral bias of neural networks. In *International conference on machine learning*, pages 5301–5310. PMLR.
- Rahimi, A. and Recht, B. (2007). Random features for large-scale kernel machines. *Advances in neural information processing systems*, 20.
- Reinert, S., Hübener, M., Bonhoeffer, T., and Goltstein, P. M. (2021). Mouse prefrontal cortex represents learned rules for categorization. *Nature*, 593(7859):411–417.

- Selvaraju, R. R., Cogswell, M., Das, A., Vedantam, R., Parikh, D., and Batra, D. (2017). Grad-cam: Visual explanations from deep networks via gradient-based localization. In *Proceedings of the IEEE international conference on computer vision*, pages 618–626.
- Shi, Z., Wei, J., and Liang, Y. (2022). A theoretical analysis on feature learning in neural networks: Emergence from inputs and advantage over fixed features. *arXiv preprint arXiv:2206.01717*.
- Simonyan, K., Vedaldi, A., and Zisserman, A. (2013). Deep inside convolutional networks: Visualising image classification models and saliency maps. *arXiv preprint arXiv:1312.6034*.
- Simonyan, K. and Zisserman, A. (2014). Very deep convolutional networks for large-scale image recognition. *arXiv preprint arXiv:1409.1556*.
- Simonyan, K. and Zisserman, A. (2015). Very deep convolutional networks for large-scale image recognition. In *3rd International Conference on Learning Representations (ICLR 2015)*. Computational and Biological Learning Society.
- Sorscher, B., Ganguli, S., and Sompolinsky, H. (2022). Neural representational geometry underlies few-shot concept learning. *Proceedings of the National Academy of Sciences*, 119(43):e2200800119.
- Stephenson, C., Padhy, S., Ganesh, A., Hui, Y., Tang, H., and Chung, S. (2021). On the geometry of generalization and memorization in deep neural networks. *arXiv preprint arXiv:2105.14602*.
- Sundararajan, M., Taly, A., and Yan, Q. (2017). Axiomatic attribution for deep networks. In *International conference on machine learning*, pages 3319–3328. PMLR.
- Vershynin, R. (2018). *High-dimensional probability: An introduction with applications in data science*, volume 47. Cambridge university press.
- Wakhloo, A. J., Sussman, T. J., and Chung, S. (2023). Linear classification of neural manifolds with correlated variability. *Physical Review Letters*.
- Yamins, D. L. and DiCarlo, J. J. (2016). Using goal-driven deep learning models to understand sensory cortex. *Nature neuroscience*, 19(3):356–365.
- Yang, G. and Hu, E. J. (2021). Tensor programs iv: Feature learning in infinite-width neural networks. In *International Conference on Machine Learning*, pages 11727–11737. PMLR.
- Zeiler, M. D. and Fergus, R. (2014). Visualizing and understanding convolutional networks. In *Computer Vision–ECCV 2014: 13th European Conference, Zurich, Switzerland, September 6-12, 2014, Proceedings, Part I 13*, pages 818–833. Springer.

A More on Related Work

Visualization. Due to the black-box and complex nature of deep neural networks, various visualization techniques have been developed to attempt to characterize the features that models learn during training (*feature visualization*) and identify which input pixel and / or feature activation in the hidden layers contribute significantly to the final model outputs (*feature attribution*). *Feature visualization* techniques visualize features (e.g convolutional filter in the case of CNNs) by generating the input sample that maximizes the activation of that given feature via gradient descent (Olah et al., 2017) (Erhan et al., 2009) (Zeiler and Fergus, 2014). With its vivid visualization, *feature visualization* provide good intuition about the qualitative characteristics of the features that DNNs learn across layers (Zeiler and Fergus, 2014) as well as different types of models (e.g, standard vs adversarially robust (Engstrom et al., 2019)). *Feature attribution* techniques generally identify how much each input and/or hidden features contribute to the final model prediction by computing the gradient of that input/hidden features to the output (some example techniques include saliency map (Simonyan et al., 2013), Grad-cam (Selvaraju et al., 2017), integrated gradient (Sundararajan et al., 2017)). Although both *feature visualization* and *feature attribution* offer intuitive understanding about the model’s feature characteristics, the qualitative nature of visualization makes it difficult to quantify the degree of relevance of the learned features to a given task.

Kernel dynamics. Kernel methods (Hofmann et al., 2008) have been classic machine learning techniques, where the primary goal is to design an effective embedding that maps inputs to a feature space, thus facilitating efficient algorithms to find good solutions (e.g., linear classifier). While neural networks are inherently complex, seminal works (Jacot et al., 2018; Lee et al., 2019) have shown that in the infinite width limit, a network can be linearized by its *neural tangent kernel (NTK)*. Thus, studying the NTK of a network allows an analytical understanding of various properties of neural networks, such as convergence to global minima (Du et al., 2018, 2019), generalization performance (Allen-Zhu et al., 2019; Arora et al., 2019), implicit bias (Bordelon et al., 2020; Canatar et al., 2021), and neural scaling laws (Bahri et al., 2021).

When a network is properly initialized (Chizat et al., 2019), gradient descent can converge to the NTK of the random initialization, a setting known as the *kernel regime* (a.k.a., *lazy training* or *random feature regime*). On the other hand, a network can also enter what is known as the *feature learning regime* (a.k.a., *rich training* or *mean-field limit*), where it deviates from the NTK of the initialization (Geiger et al., 2020). Extensive research has been conducted to characterize lazy versus rich regimes (Geiger et al., 2020) and to demonstrate instances where feature learning outperforms lazy training (Yang and Hu, 2021; Ba et al., 2022; Dandi et al., 2023). It is important to note that even when a network undergoes feature learning, the NTK can still be defined at each epoch. Previous works also analytically characterized the dynamics of kernel in simpler models (Bordelon et al., 2020). Studying such kernel dynamics also provides a lens for exploring questions related to feature learning, such as grokking (Kumar et al., 2024).

Representational geometry. The visualization approaches mentioned above focus on studying the geometric properties of the feature map itself. Another fruitful direction is to examine the geometric properties of the neural representations of inputs (i.e., embedding vectors) and their connections to performance (Chung and Abbott, 2021; Gurnani and Gajic, 2023). Various dimensionality reduction methods (e.g., principal components analysis (PCA), Isomap, t-SNE, MDS, and UMAP) have been proposed to build intuitions about the organization of high-dimensional feature spaces. In addition, there are approaches that study lower-order statistics of embedding vectors, such as representational similarity (Kriegeskorte and Kievit, 2013) and spectral methods (Rahaman

et al., 2019; Bahri et al., 2021; Ghosh et al., 2022). Methods for extracting higher-level geometric properties (e.g., dimension) have also been proposed (Chung et al., 2018; Cohen et al., 2020; Chou et al., 2025; Ansuini et al., 2019), with wide applications in both machine learning (e.g., memorization (Stephenson et al., 2021), grokking of modular arithmetic (Liu et al., 2022; Nanda et al., 2023)), in-context learning in LLM (Kirsanov et al., 2025), and neuroscience (e.g., perceptual untangling in object categorization (Chung et al., 2018), abstraction (Bernardi et al., 2020), few-shot learning (Sorscher et al., 2022), social learning (Paraouty et al., 2023)).

A.1 Previous work on storage capacity

Storage capacity is defined as the information load for linear readouts and has been studied in several communities, including learning theory (Cover, 1965) and statistical physics of neural networks (Gardner and Derrida, 1988; Gardner, 1988). To enable a mathematical treatment, we focus on the proportional limit (a.k.a. the high-dimensional limit, the thermodynamic limit), i.e., $N, P \rightarrow \infty$ and $\lim_{N, P \rightarrow \infty} N/P = O(1)$. For a given network and input data, we denote the representation of the i -th input x_i as $\Phi(x_i) \in \mathbb{R}^N$ where Φ is the (non-linear) feature map. The storage capacity of Φ is defined as.

$$\alpha(\Phi) := \lim_{N \rightarrow \infty} \max_P \left\{ \frac{P}{N} : \Pr_{\mathbf{y}} [\exists \theta \in \mathbb{R}^N, \forall i \in [P], y_i \langle \theta, \Phi(x_i) \rangle \geq 0] \geq 1 - o_N(1) \right\} \quad (\text{A.1})$$

where $\mathbf{y} \in \{\pm 1\}^P$ is uniformly random sampled, θ is the linear classifier, and $o_N(1)$ denotes vanishing terms (i.e., $o_N(1) \rightarrow 0$ as $N \rightarrow \infty$). One can also consider the setting where the distribution of \mathbf{y} is biased toward some task direction (Montanari et al., 2019). Intuitively, $\alpha(\Phi)$ quantifies the number of patterns per neuron that a network can store and decode with linear readouts.

Recall that storage capacity is defined as the critical ratio between the number of stored patterns and the number of neurons (Equation A.1). Cover’s theorem (Cover, 1965) shows that the success probability of having a linear classifier for P points with random binary labels in general position¹⁰ is $p(N, P) = 2^{1-P} \sum_{k=0}^{N-1} \binom{P-1}{k}$. In particular, for $P/N < 2$ we have $\lim_{N \rightarrow \infty} p(N, P) = 0$ and for $P/N > 2$ we have $\lim_{N \rightarrow \infty} p(N, P) = 1$. Namely, the storage capacity of points in general position with random binary label is 2. See also Figure 8 for finite-size and numerical examples.

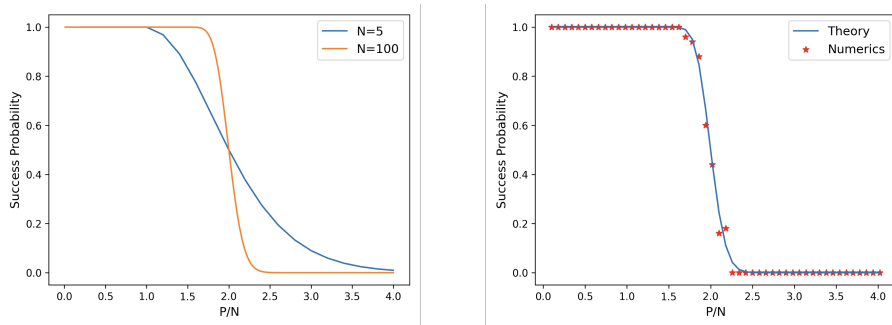


Figure 8: Storage capacity of random points and labels. Storage capacity is defined as the critical ratio $P/N = 2$ where the success probability undergoes a phase transition. Left: finite size success probability curves proved in Cover’s theorem. Right: a numerical check for Cover’s theorem.

¹⁰Meaning that every $N' \leq N$ points are linearly independent. Note that random points are in general position with probability $1 - o(1)$.

In the seminal works of Gardner and Derrida (Gardner and Derrida, 1988; Gardner, 1988), the storage capacity for random points with non-zero margin is analytically characterized using replica method. In the context of associative memory, the storage capacity of Hopfield networks (Hopfield, 1982) is calculated by (Amit et al., 1987).

B Manifold Capacity Theory and Effective Geometry

Manifold capacity theory (MCT)(Chung et al., 2018; Chung and Abbott, 2021; Wakhloo et al., 2023; Chou et al., 2025) was originally developed for the study of manifold untangling (DiCarlo and Cox, 2007) in theoretical/computational neuroscience. Intuitively, manifold untangling refers to the increased separation of high-dimensional manifolds (e.g., point cloud manifolds) in the eyes of a downstream readout. MCT quantifies this intuition via modeling a downstream neuron as a linear classifier, and uses the *packing efficiency* of the neural representational space to evaluate the degree of manifold untangling. Mathematically, such packing efficiency coincides with support vector machine (SVM) in an average-case setting.

B.1 Neural manifolds as convex hulls of pre-readout representations

As we are studying feature learning, we are interested in the neural representations that correspond to activations obtained from the pre-linear readout layer neurons. The readers can refer to Appendix D and Appendix E for details on activation extraction. Notation wise, let N be the number of neurons. Therefore, all neural representations live in \mathbb{R}^N space.

Next, we group neural representations by their category labels assigned during training to obtain P data manifolds. For $i \in \{1, \dots, P\}$, the i -th data manifold, denoted as \mathcal{M}_i , is a convex set in \mathbb{R}^N . To ensure convexity in practice, we take M_i to be the convex hull of a collection of vectors $\mathcal{M}_i = \{\mathbf{x}_1^i, \dots, \mathbf{x}_{M_i}^i\}$ where M_i is the number of points in the i -th manifold.

Notice that the each data manifold lives in its own subspace of dimension $D_i \leq N$. Therefore, we can rewrite each data manifold in its own coordinate system:

$$\mathcal{M}_i = \left\{ \mathbf{u}_0^i + \sum_{j=1}^{D_i} s_j \mathbf{u}_j^i \mid \mathbf{s} = (s_1, \dots, s_{D_i}) \in \mathcal{S}_i \right\} \quad (\text{B.1})$$

Here, \mathbf{u}_0^i is the center of the i -th manifold and $\{\mathbf{u}_j^i\}_{j=1}^{D_i}$ is an orthonormal basis. The shape set $\mathcal{S}_i \subset \mathbb{R}^{D_i}$ is a convex set denoting coordinates of the manifold points in its subspace. In practice, the manifold axes and shape sets \mathcal{S}_i are completely data driven.

B.2 A simulation definition for manifold capacity

Recall from Section 2 that the simulation version of manifold capacity is defined as follows.

Definition 2.1 (Simulated manifold capacity (Cohen et al., 2020; Chou et al., 2025)). *Let $P, N \in \mathbb{N}$ and $\mathcal{M}_i \subseteq \mathbb{R}^N$ be convex sets for each $i \in [P] = \{1, \dots, P\}$. For each $n \in [N]$, define*

$$p_n := \Pr_{\mathbf{y}, \Pi_n} [\exists \theta \in \mathbb{R}^n : y_i \langle \theta, \mathbf{s} \rangle \geq 0, \forall i \in [P], \mathbf{s} \in \mathcal{M}_i]$$

where \mathbf{y} is a random dichotomy sampled from $\{\pm 1\}^P$ and Π_n is a random projection operator from \mathbb{R}^N to \mathbb{R}^n . Suppose $p_N = 1$, the simulated capacity of $\{\mathcal{M}_i\}_{i \in [P]}$ is defined as

$$\alpha_{sim} := \frac{P}{\sum_{n \in [N]} p_n}.$$

Intuitively, the simulated manifold capacity measures the *packability* (Chung et al., 2018) of manifolds by determining the smallest dimensional subspace needed to ensure they can be separated. Namely, manifolds that are more packable¹¹ (i.e., separable when projected to smaller dimensional subspaces) exhibit higher manifold capacity. Note that the simulated capacity can be estimated from data by empirically estimate p_n and perform binary search to find the critical dimension $\min_{p_n \geq 0.5} \{n\}$. This procedure is computationally expensive and requires some choices of hyperparameters (which makes the definition a little ad hoc). Nevertheless, Definition 2.1 provides good intuition on how to think about manifold capacity (and its connection to packing).

B.3 A mean-field definition for manifold capacity

To overcome the above-mentioned drawbacks of simulated manifold capacity, previous work (Chung et al., 2018; Wakhloo et al., 2023; Chou et al., 2025) defined some *mean-field models* to enable a nice mathematical definition of manifold capacity while still being a good approximation to the simulated manifold capacity.

Mean-field model from (Chou et al., 2025). Given a collection of (finite) data manifolds $\{\mathcal{M}_i\}_{i=1}^P$. A mean-field model is to generate infinitely many (P_{mf}) manifolds in an infinite-dimensional (N_{mf}) space and characterizing the largest possible P_{mf}/N_{mf} such that these “mean-field” manifolds are separable. The key idea is that if this generating process nicely preserve the structure in the data manifolds, then the packing property of these mean-field manifolds will be very similar

Definition B.2 (Mean-field model from (Chou et al., 2025)). *Let $\{\mathcal{M}_i\}_{i \in [P]}$ be a collection of data manifolds in \mathbb{R}^N as defined in Equation B.1. Let $\alpha \in \mathbb{R}_{\geq 0}$ and P_{mf}, N_{mf} be integers with the following properties: (i) $P_{mf}, N_{mf} \rightarrow \infty$ and (ii) $P_{mf}/N_{mf} = \alpha < \infty$, and P_{mf} be divisible by P . We define the mean-field manifolds $\mathcal{M}_{mf}(P_{mf}, N_{mf}) = \{\mathcal{M}_{mf}^{a,i}\}_{a \in [P_{mf}/P], i \in [P]}$ as follows.*

- First, find an orthogonal basis $\{\mathbf{e}_k\}_{k=1}^N$ in \mathbb{R}^N for the basis vectors of all the data manifolds. Namely, for each $i \in [P]$, there exists a linear transformation $Q^i \in \mathbb{R}^{(D_i+1) \times N}$ such that $\mathbf{u}_j^i = \sum_k Q_k^{i,j} \mathbf{e}_k$ for each $j \in \{0, 1, \dots, D_i\}$.
- Next, for each $a \in [P_{mf}/P]$, generate $\mathbf{v}_1^a, \dots, \mathbf{v}_N^a \sim \mathcal{N}(0, I_{N_{mf}})$ independently and let \mathbf{V}^a be the $N_{mf} \times N$ matrix with \mathbf{v}_j^a on its columns.
- Define $M_{mf}^{a,i} = \left\{ (\mathbf{V}^a Q^i)_0 + \sum_{j=1}^{D_i} s_j (\mathbf{V}^a Q^i)_j : \mathbf{s} = (s_1, \dots, s_{D_i}) \in \mathcal{S}_i \right\}$ as the i -th manifold in the a -th cloud where $(\mathbf{V}^a Q^i)_i = \sum_k \mathbf{v}_k^a Q_k^{i,j}$ for every $a \in [P_{mf}/P]$ and $i \in [P]$.

Now, we are ready to formally define the mean-field version of manifold capacity.

Definition B.3 (Mean-field manifold capacity (Chung et al., 2018; Chou et al., 2025)). *Let $\{\mathcal{M}_i\}_{i \in [P]}$ be a collection of data manifolds in \mathbb{R}^N as defined in Equation B.1. The manifold capacity of $\{\mathcal{M}_i\}_{i \in [P]}$ is defined as*

$$\alpha_{mf} := \lim_{N_{mf} \rightarrow \infty} \max_{P_{mf}} \left\{ \frac{P_{mf}}{N_{mf}} : \Pr_{\mathbf{y}, \mathcal{M}_{mf}(P_{mf}, N_{mf})} \left[\begin{array}{c} \exists \theta \in \mathbb{R}^{N_{mf}}, \forall a \in [P_{mf}/P], i \in [P], \\ \min_{\mathbf{s} \in \mathcal{M}_{mf}^{a,i}} y_i(\theta, \mathbf{s}) \geq 0 \end{array} \right] \geq 1 - o_{N_{mf}}(1) \right\}$$

where and $o_{N_{mf}}(1) \rightarrow 0$ as $N_{mf} \rightarrow \infty$.

¹¹The reason why this is called “packing” is that projecting manifolds into smaller dimensional subspace is like packing them into a smaller neural representational space.

Finally, previous work (Chung et al., 2018; Chou et al., 2025) derived a formula for mean-field manifold capacity as follows.

$$\begin{aligned}\alpha_{\text{mf}}^{-1} &= \frac{1}{P} \mathbb{E}_{\substack{\mathbf{y} \sim \{\pm 1\}^P \\ T \sim \mathcal{N}(0, I_N)}} \left[\max_{\mathbf{s}_i \in \mathcal{M}_i} \left\{ \|\text{proj}_{\text{cone}(\{y_i \mathbf{s}_i\})} \mathbf{t}\|_2^2 \right\} \right] \\ &= \frac{1}{P} \mathbb{E}_{\substack{\mathbf{y} \sim \{\pm 1\}^P \\ T \sim \mathcal{N}(0, I_N)}} \left[\max_{\substack{\mathbf{s}_i \in \mathcal{M}_i \\ \lambda_i \geq 0}} \left\{ \left(\frac{-T \cdot \sum_i \lambda_i y_i \mathbf{s}_i}{\|\sum_i \lambda_i y_i \mathbf{s}_i\|_2} \right)_+^2 \right\} \right]\end{aligned}\tag{B.4}$$

where $\mathcal{N}(\mu, \Sigma)$ denotes the multivariate Gaussian distribution with mean μ and covariance Σ and $\text{cone}(\cdot)$ is the convex cone spanned by the vectors, i.e., $\text{cone}(\{y_i \mathbf{s}_i\}) = \{\sum_i \lambda_i y_i \mathbf{s}_i : \lambda_i \geq 0\}$.

B.4 Effective geometric measures from capacity formula

The advantages of mean-field manifold capacity are: (i) α_{mf} can be estimated via solving a quadratic program (Algorithm 1) and (ii) Equation 2.2 connects manifold capacity to the structure of the manifolds $\{\mathcal{M}_i\}$. Specifically, for each \mathbf{y}, \mathbf{t} , define $\{\mathbf{s}_i(\mathbf{y}, \mathbf{t})\} = y_i \cdot \arg \max_{\{\mathbf{s}_i\}} \|\text{proj}_{\text{cone}(\{y_i \mathbf{s}_i\})} \mathbf{t}\|_2^2$ as the *anchor points* with respect to \mathbf{y} and T . Intuitively, these anchor points are the support vectors with respect to some random projection and dichotomy as in Definition 2.1. Specifically, these anchor points are analytically linked to manifold capacity via Equation 2.2 and are distributed over the manifolds $\{\mathcal{M}_i\}$. This connection inspired the previous work (Chung et al., 2018; Chou et al., 2025) to define the following effective manifold geometric measures that capture the structure of manifolds while being analytically connected to capacity, also known as Geometry Linked to Untangling Efficiency (GLUE) (Chou et al., 2025).

The first key idea of defining effective geometric measure is the segregation of anchor points into their *center part* and their *axis part*. Concretely, for each $i \in [P]$, define $\mathbf{s}_i^0 := \mathbb{E}_{\mathbf{y}, \mathbf{t}} \{\mathbf{s}_i(\mathbf{y}, \mathbf{t})\}$ as the center of the i -th manifold and define $\mathbf{s}_i^1(\mathbf{y}, \mathbf{t}) := \mathbf{s}_i(\mathbf{y}, \mathbf{t}) - \mathbf{s}_i^0$ to be the axis part of $\mathbf{s}_i(\mathbf{y}, \mathbf{t})$ for each pair of (\mathbf{y}, \mathbf{t}) .

Next, the GLUE theory (Chou et al., 2025) used an identity: $a = \frac{b}{1 + \frac{b-a}{a}}$ inspired by (Chung et al., 2018), and set $a = \|\text{proj}_{\text{cone}(\{\mathbf{s}_i(\mathbf{y}, \mathbf{t})\}_i)} \mathbf{t}\|_2^2$ and $b = \|\text{proj}_{\text{cone}(\{\mathbf{s}_i^1(\mathbf{y}, \mathbf{t})\}_i)} \mathbf{t}\|_2^2$ to rewrite the capacity formula (Equation B.4) as follows.

$$\begin{aligned}\alpha_{\text{mf}}^{-1} &= \frac{1}{P} \mathbb{E}_{\mathbf{y}, \mathbf{t}} \left[\|\text{proj}_{\text{cone}(\{\mathbf{s}_i(\mathbf{y}, \mathbf{t})\}_i)} \mathbf{t}\|_2^2 \right] \\ &= \frac{1}{P} \mathbb{E}_{\mathbf{y}, \mathbf{t}} \left[\frac{\|\text{proj}_{\text{cone}(\{\mathbf{s}_i^1(\mathbf{y}, \mathbf{t})\}_i)} \mathbf{t}\|_2^2}{1 + \frac{\|\text{proj}_{\text{cone}(\{\mathbf{s}_i^1(\mathbf{y}, \mathbf{t})\}_i)} \mathbf{t}\|_2^2 - \|\text{proj}_{\text{cone}(\{\mathbf{s}_i(\mathbf{y}, \mathbf{t})\}_i)} \mathbf{t}\|_2^2}{\|\text{proj}_{\text{cone}(\{\mathbf{s}_i(\mathbf{y}, \mathbf{t})\}_i)} \mathbf{t}\|_2^2}} \right].\end{aligned}$$

Then, they proceeded with the following approximation.

$$\approx \frac{\frac{1}{P} \mathbb{E}_{\mathbf{y}, \mathbf{t}} \left[\|\text{proj}_{\text{cone}(\{\mathbf{s}_i^1(\mathbf{y}, \mathbf{t})\}_i)} \mathbf{t}\|_2^2 \right]}{\mathbb{E}_{\mathbf{y}, \mathbf{t}} \left[1 + \frac{\|\text{proj}_{\text{cone}(\{\mathbf{s}_i^1(\mathbf{y}, \mathbf{t})\}_i)} \mathbf{t}\|_2^2 - \|\text{proj}_{\text{cone}(\{\mathbf{s}_i(\mathbf{y}, \mathbf{t})\}_i)} \mathbf{t}\|_2^2}{\|\text{proj}_{\text{cone}(\{\mathbf{s}_i(\mathbf{y}, \mathbf{t})\}_i)} \mathbf{t}\|_2^2} \right]}.\tag{B.5}$$

(Chung et al., 2018; Chou et al., 2025) found that the above approximation empirically performs well. Furthermore, as the numerator mimics the notion of Gaussian width of a convex body and the

denominator behaves like (normalized) radius of a sphere, they defined effective manifold dimension and radius as follows.

Definition B.6 (Effective manifold geometric measures from GLUE (Chou et al., 2025)). For each $i \in [P]$, define $\mathbf{s}_i^0 := \mathbb{E}_{\mathbf{y}, \mathbf{t}}[\mathbf{s}_i(\mathbf{y}, \mathbf{t})]$ as the **center** of the i -th manifold and define $\mathbf{s}_i^1(\mathbf{y}, \mathbf{t}) := \mathbf{s}_i(\mathbf{y}, \mathbf{t}) - \mathbf{s}_i^0$ to be the **axis** part of $\mathbf{s}_i(\mathbf{y}, \mathbf{t})$ for each pair of (\mathbf{y}, \mathbf{t}) .

- **Manifold dimension** captures the degree of freedom of the noises/variations within the manifolds. Formally, it is defined as $D_{mf} := \mathbb{E}_{\mathbf{y}, \mathbf{t}}[\|\text{proj}_{\text{cone}(\{\mathbf{s}_i^1(\mathbf{y}, \mathbf{t})\}_i)} \mathbf{t}\|_2^2]$.
- **Manifold radius** captures the noise-to-signal ratio of the manifolds. Formally, it is defined as $R_{mf} := \sqrt{\mathbb{E}_{\mathbf{y}, \mathbf{t}} \left[\frac{\|\text{proj}_{\text{cone}(\{\mathbf{s}_i(\mathbf{y}, \mathbf{t})\}_i)} \mathbf{t}\|^2}{\|\text{proj}_{\text{cone}(\{\mathbf{s}_i^1(\mathbf{y}, \mathbf{t})\}_i)} \mathbf{t}\|^2 - \|\text{proj}_{\text{cone}(\{\mathbf{s}_i(\mathbf{y}, \mathbf{t})\}_i)} \mathbf{t}\|^2} \right]}$.
- **Center alignment** captures the correlation between the center of different manifolds. Formally, it is defined as $\rho_{mf}^c := \frac{1}{P(P-1)} \sum_{i \neq j} |\langle \mathbf{s}_i^0, \mathbf{s}_j^0 \rangle|$.
- **Axis alignment** captures the correlation between the axis of different manifolds. Formally, it is defined as $\rho_{mf}^a := \frac{1}{P(P-1)} \sum_{i \neq j} \mathbb{E}_{\mathbf{y}, \mathbf{t}}[|\langle \mathbf{s}_i^1(\mathbf{y}, \mathbf{t}), \mathbf{s}_j^1(\mathbf{y}, \mathbf{t}) \rangle|]$.
- **Center-axis alignment** captures the correlation between the center and axis of different manifolds. Formally, it is defined as $\psi_{mf} := \frac{1}{P(P-1)} \sum_{i \neq j} \mathbb{E}_{\mathbf{y}, \mathbf{t}}[|\langle \mathbf{s}_i^0, \mathbf{s}_j^1(\mathbf{y}, \mathbf{t}) \rangle|]$.

A capacity approximation formula by dimension and radius. Recall that in Equation B.5 previous work (Chung et al., 2018) used the identity $a = \frac{b}{1 + \frac{b-a}{a}}$ to approximate the manifold capacity. After defining manifold dimension and radius, one can then plug them back to Equation B.5 and get the following approximation of manifold capacity via effective manifold dimension and radius.

$$\alpha_{mf} \approx \frac{1 + R_{mf}^{-2}}{D_{mf}}. \quad (\text{B.7})$$

B.5 Connections between manifold capacity and its effective geometric measures

Here, we demonstrate the connections between manifold capacity and its effective geometric measures by synthetic manifolds. In particular, we consider isotropic Gaussian clouds parametrized by a set of *ground truth* latent parameters: dimension D_{ground} , radius R_{ground} , center correlations ρ_{ground}^c , axis correlations ρ_{ground}^a , and center-axis correlations ψ_{ground} . See subsection D.1.1 for more details on the generative process. In this section, we focus on showing that the effective geometric measures $D_{mf}, R_{mf}, \rho_{mf}^c, \rho_{mf}^a, \psi_{mf}$ capture the corresponding ground truth parameter.

Effective manifold dimension and radius. We first set all the manifold correlations to be zero and vary the ground truth radius and dimension. Here we pick $N = 1000$ neurons, $P = 2$ manifold, $M = 200$ points per manifold, varying the underlying dimension from 2 to 10, and varying the underlying radius from 0.8 to 2. In Figure 9, we vary the ground truth dimension in the x-axis, and in Figure 10, we vary the ground truth radius in the x-axis.

Effective alignment measures. Next, we fix the ground truth dimension to be $D_{\text{ground}} = 4$ and radius to be $R_{\text{ground}} = 1$ and vary $\rho_{\text{ground}}^c, \rho_{\text{ground}}^a, \psi_{\text{ground}}$ from 0 to 0.8. In Figure 11, we vary the center correlations, and in Figure 12, we vary the axis correlations.

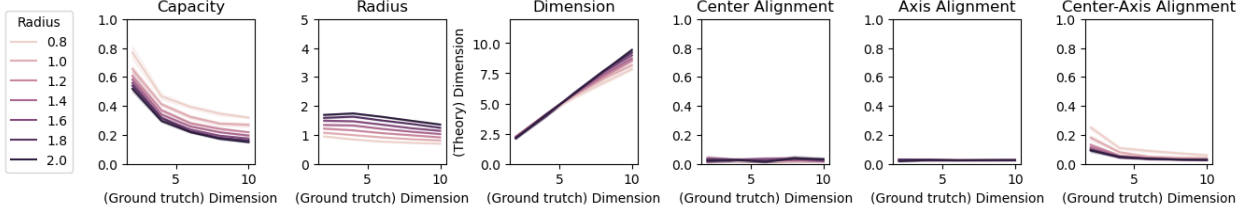


Figure 9: Effective manifold dimension tracks the ground truth dimension of uncorrelated isotropic Gaussian clouds. Note that the higher the dimension, the smaller capacity, as discussed in Figure 3c.

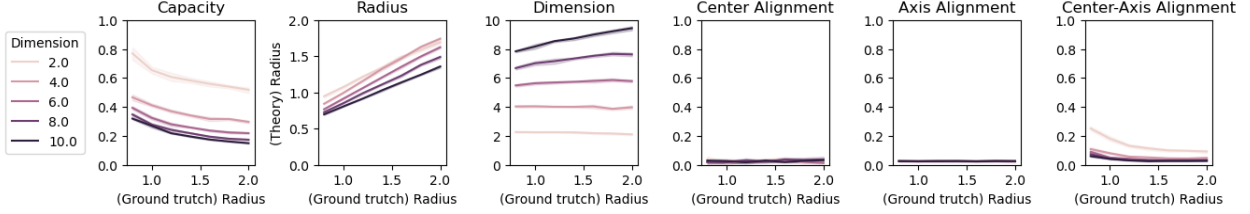


Figure 10: Effective manifold radius tracks the ground truth radius of uncorrelated isotropic Gaussian clouds. Note that the higher the radius, the smaller capacity, as discussed in Figure 3c.

B.6 Algorithms for estimating manifold capacity and effective geometric measure

We provide pseudocodes for estimating manifold capacity and effective geometric measure in Algorithm 1.

C Theoretical Results

C.1 Formal statement of Theorem 3.1

Let $d \in \mathbb{N}$ be the input dimension and $N \in \mathbb{N}$ be the number of hidden units. Let $W_0 \in \mathbb{R}^{N \times d}$ be the weight matrix of a fully connected 2-layer neural network. The feature of an input vector is defined as $\Phi_0(\mathbf{x}) = \sigma(W_0 \mathbf{x})$ where $\sigma(\cdot) : \mathbb{R} \rightarrow \mathbb{R}$ is a non-linear activation function, e.g., ReLU or tanh. The readout weight is denoted as $\mathbf{a} \in \mathbb{R}^N$. Finally, the output of the 2-layer NN is the sign of the readout, i.e., $f(\mathbf{x}) = \text{sgn}(\mathbf{a}^\top \Phi(\mathbf{x}))$.

Let $\{(\mathbf{x}_i, y_i)\}_{i \in [P_{\text{train}}]}$ be the collection of training data. We consider gradient descent over the mean square error (MSE) of the 2-layer NN, i.e., $L(f) = \frac{1}{P_{\text{train}}} \sum_{i \in [P_{\text{train}}]} \ell(f(\mathbf{x}_i), y_i)$ where $\ell(z_i, y_i) = \frac{1}{2}(z - y)^2$. The gradient update with learning rate $\eta > 0$ is $W_{t+1} = W_t + \eta G_t$ where

$$G_t = \frac{1}{P_{\text{train}}} \sum_{i \in [P_{\text{train}}]} \left[(y_i - \mathbf{a}^\top \sigma(W_t \mathbf{x}_i)) \mathbf{a} \odot \sigma'(W_t \mathbf{x}_i) \right] \mathbf{x}_i^\top$$

and $\sigma'(\cdot)$ denotes the first order derivative of $\sigma(\cdot)$.

Assumption C.1. We adopt the following assumptions used in (Montanari et al., 2019; Ba et al., 2022).

1. (Proportional limit) $P_{\text{train}}, d, N \rightarrow \infty$ with $\psi_1 = N/d$, $\psi_2 = P_{\text{train}}/d$, and $0 < \psi_1, \psi_2 < \infty$.
2. (Gaussian initialization) $[W_0]_{kj} \sim \mathcal{N}(0, 1/N)$ for each $k \in [N]$ and $j \in [d]$.

Algorithm 1 Estimate manifold capacity and effective geometric measures

Input: $\{\mathcal{M}_i\}$: P point clouds, each containing M points in an N -dimensional ambient space; n_t : number of samples for estimating the expectation.

Output: α_{mf} : Manifold capacity; D_{mf} : Effective dimension; R_{mf} : Effective radius; ρ_{mf}^a : Effective axis alignment; ρ_{mf}^c : Effective center alignment; ψ_{mf} : Effective center-axis alignment.

% Step 1: Sample anchor points.

for k from 1 to n_t **do**

$\mathbf{t}_k \leftarrow$ a vector sampled from isotropic N -dimensional Gaussian distribution.

$\mathbf{y} \leftarrow$ a random dichotomy vector from $\{\pm 1\}^P$.

$\mathbf{A} \leftarrow I_N$; $\mathbf{q} \leftarrow -\mathbf{t}_k$; $\mathbf{h} \leftarrow \mathbf{0}_N$.

$\mathbf{G} \leftarrow (y \odot \{\mathcal{M}_i\}_{i=1}^P)$. $\triangleright \mathbf{G}_{i,j} = y_i \mathbf{s}$ is a row vector where \mathbf{s} is the j -th point in \mathcal{M}_i .

 output $\leftarrow qp(\mathbf{A}, \mathbf{q}, \mathbf{G}, \mathbf{h})$. $\triangleright \min_{\mathbf{x}} \frac{1}{2} \mathbf{x}^\top \mathbf{A} \mathbf{x} + \mathbf{q}^\top \mathbf{x}$ s.t. $\mathbf{G} \mathbf{x} \leq \mathbf{h}$.

$\mathbf{z}_{\text{dual}} \leftarrow$ output["dual"]

\triangleright The support vectors

for i from 1 to P **do**

$\mathbf{s}_i[k] \leftarrow \sum_j (\mathbf{z}_{\text{dual}})_{i,j}^\top \mathbf{G} / \sum_j (\mathbf{z}_{\text{dual}})_{i,j}$

% Step 2: Estimate (anchor) manifold centers.

for i from 1 to P **do**

$\mathbf{s}_i^0 \leftarrow \frac{1}{n_t} \sum_{k=1}^{n_t} \mathbf{s}_i[k]$.

$\mathbf{G}^0 \leftarrow \sum_i \mathbf{s}_i^0 (\mathbf{s}_i^0)^\top$.

\triangleright Anchor center gram matrix.

% Step 3: Separate the center and axis part of anchor points.

for k from 1 to n_t **do**

for i from 1 to P **do**

$\mathbf{s}_i^1[k] \leftarrow \mathbf{s}_i[k] - \mathbf{s}_i^0$. \triangleright The axis part of the anchor point in the i -th manifold.

$\mathbf{t}^1[k] \leftarrow \sum_i \mathbf{s}_i^1[k] \mathbf{t}_k$.

$\mathbf{G}^1[k] \leftarrow \sum_i \mathbf{s}_i^1[k] (\mathbf{s}_i^1[k])^\top$.

\triangleright Anchor axis gram matrix.

% Step 4: Estimate manifold capacity and effective geometric measures.

$\alpha_{\text{mf}} \leftarrow \left(\frac{1}{n_t P} \sum_{k=1}^{n_t} (\mathbf{s}_i[k] \mathbf{t}_k)^\top (\mathbf{s}_i[k] (\mathbf{s}_i[k])^\top)^\dagger (\mathbf{s}_i[k] \mathbf{t}_k) \right)^{-1}$.

$D_{\text{mf}} \leftarrow \frac{1}{n_t P} \sum_{k=1}^{n_t} \mathbf{t}^1[k]^\top \mathbf{G}^1[k] \mathbf{t}^1[k]$.

$R_{\text{mf}} \leftarrow \sqrt{\frac{1}{n_t} \sum_{k=1}^{n_t} \frac{\mathbf{t}^1[k]^\top (\mathbf{G}^1[k] + \mathbf{G}^0) \mathbf{t}^1[k]}{\mathbf{t}^1[k]^\top (\mathbf{G}^1[k] + \mathbf{G}^1[k]) (\mathbf{G}^0)^\dagger \mathbf{G}^1[k] (\mathbf{G}^0)^\dagger \mathbf{t}^1[k]}}$. \triangleright Equivalent to the definition of radius after applying the Woodbury formula for numerical stability.

$\rho_{\text{mf}}^c \leftarrow \frac{1}{P(P-1)} \sum_{i=1}^P \sum_{i \neq j} \frac{(\mathbf{s}_i^0)^\top \mathbf{s}_j^0}{\|\mathbf{s}_i^0\|_2 \cdot \|\mathbf{s}_j^0\|_2}$.

$\rho_{\text{mf}}^a \leftarrow \frac{1}{P(P-1)} \sum_{i=1}^P \sum_{j \neq i} \frac{1}{n_k} \sum_{k=1}^{n_k} \frac{\mathbf{s}_i^1[k]^\top \mathbf{s}_j^1[k]}{\|\mathbf{s}_i^1[k]\|_2 \cdot \|\mathbf{s}_j^1[k]\|_2}$.

$\psi_{\text{mf}} \leftarrow \frac{1}{P(P-1)} \sum_{i=1}^P \sum_{j \neq i} \frac{1}{n_k} \sum_{k=1}^{n_k} \frac{(\mathbf{s}_i^0)^\top \mathbf{s}_j^1[k]}{\|\mathbf{s}_i^0\|_2 \cdot \|\mathbf{s}_j^1[k]\|_2}$.

return $\alpha_{\text{mf}}, D_{\text{mf}}, R_{\text{mf}}, \rho_{\text{mf}}^a, \rho_{\text{mf}}^c, \psi_{\text{mf}}$.

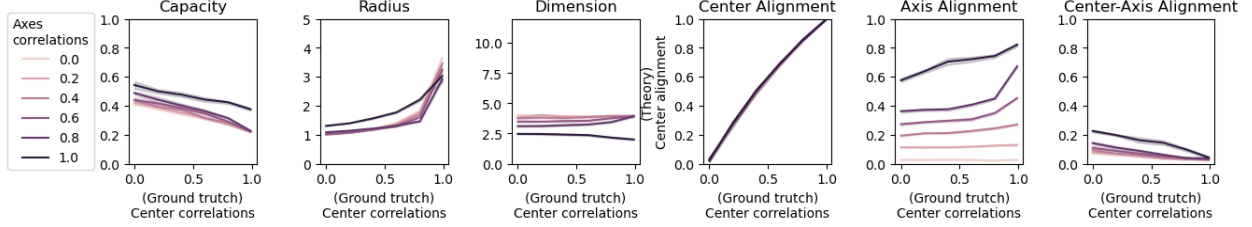


Figure 11: Effective manifold center alignment tracks the ground truth center correlations of isotropic Gaussian clouds. Note that the higher the center alignment, the smaller capacity, as discussed in Figure 3c. Also, in the large center correlations regime, the effective radius increases.

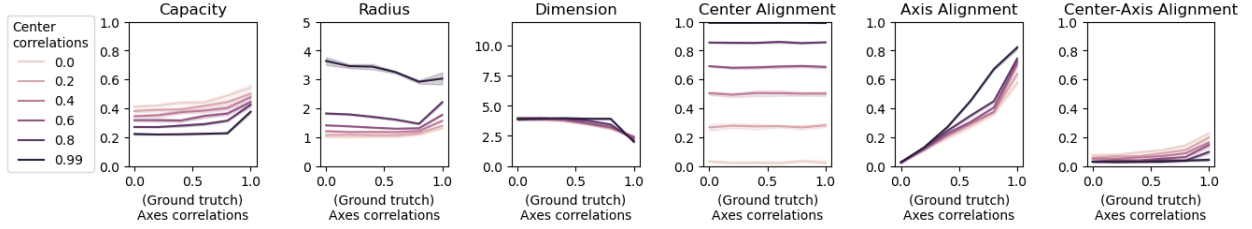


Figure 12: Effective manifold axis alignment tracks the ground truth axis correlations of isotropic Gaussian clouds. Note that the higher the axis alignment, the higher capacity, as discussed in Figure 3c. Also, in the large axis correlations regime, the effective dimension decreases.

3. (Gaussian readout) $a_k \sim \mathcal{N}(0, 1/N)$ for each $k \in [N]$.
4. (Normalized activation) The non-linear activation function $\sigma(\cdot)$ has $O(1)$ -bounded first three derivatives almost surely. In addition, $\mathbb{E}[\sigma(G)] = 0$ and $\mathbb{E}[G\sigma(G)] \neq 0$ for $G \sim \mathcal{N}(0, 1)$.
5. (Non-degenerate label function) Let $F : \mathbb{R} \rightarrow [0, 1]$ be a continuous function satisfying

$$\inf\{x : \Pr[T < x] > 0\} = -\infty \quad \text{and} \quad \sup\{x : \Pr[T > x] > 0\} = \infty$$

where $T = YG$, $G \sim \mathcal{N}(0, 1)$, and $\Pr[Y = 1 | G] = 1 - \Pr[Y = -1 | G] = F(G)$.

Setting C.2. We consider the following data generation process. Let $F : \mathbb{R} \rightarrow [0, 1]$ be a function satisfying Assumption C.1. Let $\beta_* \in \mathbb{R}^d$ be a hidden vector with $\|\beta_*\|_2 = 1$. The data distribution $\mathcal{D}_F(\beta_*)$ is defined by the following two steps: (i) sample $\mathbf{x} \sim \mathcal{N}(0, I_d)$, and (ii) sample y with $\Pr[y = 1] = 1 - \Pr[y = -1] = F(\langle \beta_*, \mathbf{x} \rangle)$. Finally, the prediction accuracy of a network is defined as the expected accuracy of a fresh sample, i.e., $\Pr_{(\mathbf{x}, y) \sim \mathcal{D}_F(\beta_*)}[yf(\mathbf{x}) \geq 0]$.

Parameter C.3. Given $\psi_1, \psi_2, F, \beta_*$ from Assumption C.1 and Setting C.2. We define the follow-

ing parameters.

$$\begin{aligned}
\gamma_1 &= \mathbb{E}_{G \sim \mathcal{N}(0,1)} [G\sigma(G)] \\
\gamma_2^2 &= \mathbb{E}_{G \sim \mathcal{N}(0,1)} [\sigma(G)^2] - \mathbb{E}_{G \sim \mathcal{N}(0,1)} [G\sigma(G)]^2 \\
\theta_1 &= \mathbb{E}_{X \sim \mu_{\psi_1}} \left[\frac{\gamma_1^2}{\gamma_1^2 X + \gamma_2^2} \right] \\
\theta_2 &= \psi_1 \mathbb{E}_{X \sim \mu_{\psi_1}} \left[\frac{\gamma_1^2 X}{\gamma_1^2 X + \gamma_2^2} \right] \\
\theta_3 &= \mathbb{E}_{(G,Y) \sim \mathcal{D}_F} [YG] \\
\theta_4 &= \left(\frac{1}{\psi_2} + \mathbb{E}_{(G,Y),(G',Y') \stackrel{i.i.d.}{\sim} \mathcal{D}_F} [YY'GG'] \right)
\end{aligned}$$

where μ_{ψ_1} is the Marchenko-Pastur distribution with the ratio parameter being ψ_1 and $(G, Y) \sim \mathcal{D}_F$ is defined as the sampling process: $G \sim \mathcal{N}(0, 1)$ and $\Pr[Y = 1] = 1 - \Pr[Y = -1] = F(G)$.

Theorem C.4. Given *Assumption C.1* and consider $0 < \psi_1, \psi_2, \eta < \infty$.

- (Capacity tracks the degree of feature learning) The storage capacity of 2-layer network trained with synthetic data defined in *Setting C.2* after one gradient step is $\alpha_{P_{\text{train}}, d, N}(\psi_1, \psi_2, \eta)$ and

$$\alpha_{P_{\text{train}}, d, N}(\psi_1, \psi_2, \eta) \xrightarrow{P_{\text{train}}, d, N \rightarrow \infty} \alpha(\psi_1, \psi_2, \eta)$$

Here the function $\alpha(\cdot)$ is defined as

$$\alpha(\psi_1, \psi_2, \eta) = \left(\min_{c \in \mathbb{R}} \mathbb{E}_{(Z, G, Y) \sim \mathcal{D}_{\psi_1, \psi_2, \eta}} [(-cYG - Z)_+^2] \right)^{-1}$$

where $(Z, G, Y) \sim \mathcal{D}_{\psi_1, \psi_2, \eta}$ is defined as the following sampling process

$$Z \sim \mathcal{N}(0, 1), \quad G \sim \mathcal{N}(0, 1), \quad \Pr[Y = 1] = 1 - \Pr[Y = -1] = f_{\tau(\psi_1, \psi_2, \eta)}(G)$$

and the scalar function $f_{\tau}(\cdot)$ and $\tau(\psi_1, \psi_2, \eta)$ are defined as

$$f_{\tau}(G) = \mathbb{E}_{G' \sim \mathcal{N}(0,1)} \left[F(\sqrt{1 - \tau^2}G + \tau G') \right]$$

and

$$\tau = \tau(\psi_1, \psi_2, \eta) = \sqrt{\tau_0(\psi_1, \psi_2)^2 - \tau_{\Delta}(\psi_1, \psi_2, \eta)^2}$$

where $\tau_0(\cdot)$ and $\tau_{\Delta}(\cdot)$ are scalar functions defined as

$$\tau_0(\psi_1, \psi_2)^2 = 1 - \theta_2$$

and

$$\tau_{\Delta}(\psi_1, \psi_2, \eta)^2 = \frac{\eta^2 \theta_1 (1 - \theta_2)^2 \theta_3^2}{1 + \eta^2 \theta_1 (1 - \theta_2) \theta_4}$$

where the parameters θ_i 's are defined in *Parameter C.3*. In particular, $0 < \alpha(\psi_1, \psi_2, \eta) < \alpha(\psi_1, \psi_2, \eta')$ for all $0 < \eta < \eta'$.

2. (Capacity analytically links to prediction accuracy) The prediction accuracy of 2-layer network trained with synthetic data defined in [Setting C.2](#) after one gradient step is $\text{Acc}_{P_{\text{train}},d,N}(\psi_1, \psi_2, \eta)$ and

$$\text{Acc}_{P_{\text{train}},d,N}(\psi_1, \psi_2, \eta) \xrightarrow{P_{\text{train}},d,N \rightarrow \infty} \text{Acc}(\psi_1, \psi_2, \eta)$$

Here the function $\text{Acc}(\cdot)$ is defined as

$$\text{Acc}(\psi_1, \psi_2, \eta) = \mathbb{E}_{(G,Y) \sim \mathcal{D}_F} \left[\Phi \left(\frac{\eta \gamma_1^2 \theta_3}{\sqrt{\frac{\eta^2 \gamma_1^4}{\psi_2} + \gamma_1^2 + \gamma_*^2}} YG \right) \right]$$

In particular, there exists an increasing and invertible function $g_{\psi_1, \psi_2} : [0, 1] \rightarrow \mathbb{R}_+$ such that

$$\text{Acc}(\psi_1, \psi_2, \eta) = g_{\psi_1, \psi_2}(\alpha(\psi_1, \psi_2, \eta)).$$

C.2 Proof for Theorem C.4

Step 1: Rank-1 approximation of gradient descent in 2-layer networks by ref. (Ba et al., 2022). When the learning rate is constant, i.e., $\eta = O(1)$, ref. (Ba et al., 2022) shows that the gradient update matrix can be approximated by a rank-1 matrix. In particular, the following is a restatement of Proposition 2 in (Ba et al., 2022).

Proposition C.5 (Proposition 2 in (Ba et al., 2022)). *Given Assumption C.1 and Setting C.2, there exist some constants $c, C > 0$ such that for all large P_{train}, N, d , the following holds*

$$\left\| G_0 - \gamma_1 \mathbf{a} \left(\frac{\sum_i y_i \mathbf{x}_i^\top}{P_{\text{train}}} \right) \right\| \leq \frac{C \log^2 P_{\text{train}}}{\sqrt{P_{\text{train}}}} \cdot \|G_0\|$$

with probability at least $1 - P_{\text{train}} e^{-c \log^2 P_{\text{train}}}$ and $\|\cdot\|$ denotes the operator norm.

Step 2: A formula for the storage capacity of a Gaussian model by ref. (Montanari et al., 2019). The storage capacity of a Gaussian model is proven in (Montanari et al., 2019). In particular, the following is a restatement of the Proposition 5.1 in (Montanari et al., 2019).

Definition C.6 (Gaussian model). *Let $\theta_* \in \mathbb{R}^N$ be some latent vector. A sample $(\mathbf{x}_i, y_i) \in \mathbb{R}^N \times \{\pm 1\}$ is i.i.d. sampled as follows. First, sample \mathbf{x}_i from $\mathcal{N}(0, \Sigma)$ where Σ is a covariance matrix satisfying certain technical condition as defined in Assumption 1-2 in (Montanari et al., 2019). Next, let $y_i = +1$ with probability $f(\langle \theta_*, \mathbf{x}_i \rangle)$ for some function f satisfying Assumption 3 in (Montanari et al., 2019).*

Proposition C.7 (Theorem 3 in (Montanari et al., 2019)). *Consider a Gaussian model satisfying Definition C.6. As $P_{\text{train}}, N, d \rightarrow \infty$, the storage capacity converges to*

$$\alpha^* = \left(\min_{c \in \mathbb{R}} \mathbb{E}_{(Z,G,Y) \sim \mathcal{D}_f} [(-cYG - Z)_+]^2 \right)^{-1}$$

where $(Z, G, Y) \sim \mathcal{D}_f$ is defined as the following sampling process

$$Z \sim \mathcal{N}(0, 1), \quad G \sim \mathcal{N}(0, 1), \quad \Pr[Y = 1] = 1 - \Pr[Y = -1] = f(\rho \cdot G).$$

where ρ is some scalar related to the Gaussian model as defined in Assumption 2 of (Montanari et al., 2019).

Note that the capacity only depends on the alignment between data and task (as encoded in f) and does not depend on the covariance structure. The dependence on the covariance structure will appear when one considers the non-zero margin version of capacity.

Step 3: A Gaussian equivalent model for 2-layer NNs after one gradient step. Next, we combine a Gaussian equivalent model for random feature 2-layer NNs in (Montanari et al., 2019) (Theorem 3) and the rank-1 approximation of gradient step in Proposition C.5 to get a Gaussian equivalent model for 2-layer NNs after one gradient step.

Proposition C.8. *Given Assumption C.1 and $0 < \psi_1, \psi_2, \eta < \infty$. Let $d \in \mathbb{N}$ and (W_1, β_*, F) be the weight matrix, hidden vector, and label function from Setting C.2. Let $\alpha_{P_{train,d,N}}^{GM}(\psi_1, \psi_2, \eta)$ be the capacity of the following Gaussian model:*

$$\begin{aligned}
\Sigma_{d,\eta} &= \gamma_1^2 W_1 W_1^\top + \gamma_*^2 I \\
\theta_{*,d,\eta} &= \alpha_{d,\eta}^{-1} \gamma_1 (\gamma_1^2 W_1 W_1^\top + \gamma_*^2 I)^{-1} W_1 \beta_* \\
\alpha_{d,\eta}^2 &= \gamma_1^2 \beta_*^\top W_1^\top (\gamma_1^2 W_1 W_1^\top + \gamma_*^2 I)^{-1} W_1 \beta_* \\
\tau_{d,\eta}^2 &= 1 - \alpha_{d,\eta}^2 \\
f_{d,\eta}(x) &= \mathbb{E}_{G \sim \mathcal{N}(0,1)} [F(\alpha_{d,\eta} x + \tau_{d,\eta} G)].
\end{aligned} \tag{C.9}$$

We have that

$$\lim_{P_{train,d,N} \rightarrow \infty} |\alpha_{P_{train,d,N}}(\psi_1, \psi_2, \eta) - \alpha_{P_{train,d,N}}^{GM}(\psi_1, \psi_2, \eta)| = 0$$

and

$$\alpha_{P_{train,d,N}}^{GM}(\psi_1, \psi_2, \eta) \xrightarrow{P_{train,d,N} \rightarrow \infty} \alpha(\psi_1, \psi_2, \eta).$$

Here the function $\alpha(\cdot)$ is defined as

$$\alpha(\psi_1, \psi_2, \eta) = \left(\min_{c \in \mathbb{R}} \mathbb{E}_{(Z,G,Y) \sim \mathcal{D}_{f_\tau(\psi_1, \psi_2, \eta)}} [(-cYG - Z)_+^2] \right)^{-1}$$

where the scalar function $f_\tau(\cdot)$ and $\tau(\psi_1, \psi_2, \eta)$ are defined as

$$f_\tau(G) = \mathbb{E}_{G' \sim \mathcal{N}(0,1)} [F(\sqrt{1 - \tau^2} G + \tau G')]$$

and

$$\tau = \tau(\psi_1, \psi_2, \eta) = \lim_{d \rightarrow \infty} \tau_{d,\eta} = \sqrt{\tau_0(\psi_1, \psi_2)^2 - \tau_\Delta(\psi_1, \psi_2, \eta)^2}.$$

where $\tau_0(\psi_1, \psi_2) = \lim_{d \rightarrow \infty} \tau_{d,0}$.

To derive the Gaussian equivalent model in Proposition C.8 of the random features model after one gradient step defined in Setting C.2, we analyze the following random features and their associated labels:

$$\Phi_0(\mathbf{x}_i) = \sigma(W_1 \mathbf{x}_i), \quad \Pr[y_i = 1 | \mathbf{x}_i] = 1 - \Pr[y_i = -1 | \mathbf{x}_i] = F(\langle \beta_*, \mathbf{x}_i \rangle), \quad \|\beta_*\|_2 = 1$$

where $\mathbf{x}_i \sim \mathcal{N}(0, I_d)$ and $W_1 = W_0 + \eta G_0$ while G_0 satisfies the bound given in Proposition C.5. Given the assumptions in Assumption C.1, we can decompose the nonlinear activation function σ into Hermite polynomials. Following our parameters in Parameter C.3, we define the Gaussian equivalent features of our model as the linearization of Equation C.2:

$$\mathbf{g}_i = \gamma_1 W_1 \mathbf{x}_i + \gamma_2 \mathbf{h}_i$$

where $\mathbf{h}_i \sim \mathcal{N}(0, I_N)$ are independent from everything else. Now, we wish to find a similar linearized Gaussian model for the labels y_i given the Gaussian equivalent features \mathbf{g}_i . It is easy to check that the Gaussian features has the following covariance:

$$\mathbf{g}_i \sim \mathcal{N}(0, \Sigma_{d,\eta}), \quad \Sigma_{d,\eta} = \gamma_1^2 W_1 W_1^\top + \gamma_*^2 I$$

By matching covariance through [Equation C.2](#), we obtain

$$\mathbf{x}_i = \gamma_1 W_1^\top \Sigma_{d,\eta}^{-1} \mathbf{g}_i + Q^{1/2} \tilde{\mathbf{h}}_i$$

where $Q = \gamma_2^2 (\gamma_2^2 I_N + \gamma_1^2 W_1^\top W_1)^{-1}$ and $\tilde{\mathbf{h}}_i \sim \mathcal{N}(0, I_N)$ are independent of \mathbf{x}_i . Therefore, we can rewrite the label function parameter as

$$\langle \beta_*, \mathbf{x}_i \rangle = \alpha_{d,\eta} \langle \theta_{*,d,\eta}, \mathbf{g}_i \rangle + \varepsilon_i$$

where $\varepsilon_i \sim \mathcal{N}(0, \tau_{d,\eta}^2)$ are independent of \mathbf{g}_i . Effectively, we obtain an equivalent label function

$$f_{d,\eta}(x) = \mathbb{E}_{G \sim \mathcal{N}(0,1)} [F(\alpha_{d,\eta} x + \tau_{d,\eta} G)]$$

such that $\Pr[y_i = 1 | \mathbf{x}_i] = 1 - \Pr[y_i = -1 | \mathbf{x}_i] = f_{d,\eta}(\langle \theta_{*,d,\eta}, \mathbf{g}_i \rangle)$. It is easy to verify that this Gaussian model satisfies the assumptions in [Definition C.6](#).

Step 4: Analysis of τ . Finally, we combine [Proposition C.5](#) and [Proposition C.8](#) to get the formula for the right hand side of [Equation C.9](#). From [Proposition C.5](#), we approximate W_1 as $W_1 = W_0 + \mathbf{a} \mathbf{u}^\top$ where $\mathbf{u} = \eta \sum_i y_i \mathbf{x}_i^\top / P_{\text{train}}$. To rewrite the right hand side of [Equation C.9](#), we first deal with the matrix inverse term using the same trick as in ref. ([Ba et al., 2022](#)). Let $\Sigma_t = \gamma_1^2 W_t W_t^\top + \gamma_*^2 I$. Observe that

$$\Sigma_1 = \Sigma_0 + \gamma_1^2 \begin{bmatrix} \mathbf{a} & \mathbf{c} \end{bmatrix} \begin{bmatrix} L_1 & 1 \\ 1 & 0 \end{bmatrix} \begin{bmatrix} \mathbf{a}^\top \\ \mathbf{c}^\top \end{bmatrix}$$

where $\mathbf{c} = W_0 \mathbf{u}$. By Sherman-Morrison-Woodbury formula, we have

$$\begin{aligned} \Sigma_1^{-1} &= \Sigma_0^{-1} - \gamma_1^2 \Sigma_0^{-1} \begin{bmatrix} \mathbf{a} & \mathbf{c} \end{bmatrix} \left(\begin{bmatrix} L_1 & 1 \\ 1 & 0 \end{bmatrix}^{-1} + \gamma_1^2 \begin{bmatrix} \mathbf{a}^\top \\ \mathbf{c}^\top \end{bmatrix} \Sigma_0^{-1} \begin{bmatrix} \mathbf{a} & \mathbf{c} \end{bmatrix} \right)^{-1} \begin{bmatrix} \mathbf{a}^\top \\ \mathbf{c}^\top \end{bmatrix} \Sigma_0^{-1} \\ &= \Sigma_0^{-1} - \Delta_{aa} - \Delta_{cc} + \Delta_{ac} + \Delta_{ca} \end{aligned}$$

where

$$\begin{aligned} \Delta_{aa} &= \gamma_1^2 \frac{L_4 - L_1}{D} \Sigma_0^{-1} \mathbf{a} \mathbf{a}^\top \Sigma_0^{-1} \\ \Delta_{cc} &= \gamma_1^2 \frac{L_3}{D} \Sigma_0^{-1} \mathbf{c} \mathbf{c}^\top \Sigma_0^{-1} \\ \Delta_{ac} &= \gamma_1^2 \frac{1 + L_6}{D} \Sigma_0^{-1} \mathbf{a} \mathbf{c}^\top \Sigma_0^{-1} \\ \Delta_{ca} &= \gamma_1^2 \frac{1 + L_6}{D} \Sigma_0^{-1} \mathbf{c} \mathbf{a}^\top \Sigma_0^{-1} \end{aligned}$$

and

$$\begin{aligned}
L_0 &= \gamma_1^2 \beta_*^\top W_0^\top \Sigma_0^{-1} W_0 \beta_* \\
L_1 &= \mathbf{u}^\top \mathbf{u} \\
L_2 &= \mathbf{u}^\top \beta_* \\
L_3 &= \gamma_1^2 \mathbf{a}^\top \Sigma_0^{-1} \mathbf{a} \\
L_4 &= \gamma_1^2 \mathbf{c}^\top \Sigma_0^{-1} \mathbf{c} \\
L_5 &= \gamma_1^2 \mathbf{c}^\top \Sigma_0^{-1} W_0 \beta_* \\
L_6 &= \gamma_1^2 \mathbf{a}^\top \Sigma_0^{-1} \mathbf{c} \\
L_7 &= \mathbf{a}^\top \mathbf{c} \\
L_8 &= \gamma_1^2 \mathbf{a}^\top \Sigma_0^{-1} W_0 \beta_* \\
D &= L_3(L_4 - L_1) - (1 + L_6)^2
\end{aligned}$$

Thus, we can rewrite the right hand side of [Equation C.9](#) as follows.

$$\begin{aligned}
\tau_{d,\eta} &= 1 - \gamma_1^2 \beta_*^\top (W_0 + \mathbf{a} \mathbf{u}^\top)^\top \Sigma_0^{-1} (W_0 + \mathbf{a} \mathbf{u}^\top) \beta_* \\
&\quad + \gamma_1^2 \beta_*^\top (W_0 + \mathbf{a} \mathbf{u}^\top)^\top \Delta_{aa} (W_0 + \mathbf{a} \mathbf{u}^\top) \beta_* \\
&\quad + \gamma_1^2 \beta_*^\top (W_0 + \mathbf{a} \mathbf{u}^\top)^\top \Delta_{cc} (W_0 + \mathbf{a} \mathbf{u}^\top) \beta_* \\
&\quad - \gamma_1^2 \beta_*^\top (W_0 + \mathbf{a} \mathbf{u}^\top)^\top \Delta_{ac} (W_0 + \mathbf{a} \mathbf{u}^\top) \beta_* \\
&\quad - \gamma_1^2 \beta_*^\top (W_0 + \mathbf{a} \mathbf{u}^\top)^\top \Delta_{ca} (W_0 + \mathbf{a} \mathbf{u}^\top) \beta_* \\
&= 1 - L_0 - L_2^2 L_3 - 2L_2 L_8 \\
&\quad + \frac{L_4 - L_1}{D} (L_2 L_3 + L_8)^2 \\
&\quad + \frac{L_3}{D} (L_5 + L_2 L_6)^2 \\
&\quad - 2 \frac{1 + L_6}{D} (L_2 L_3 + L_8) (L_5 + L_2 L_6).
\end{aligned}$$

Similar to Proposition 29 in [\(Ba et al., 2022\)](#), by Hanson-Wright inequality, we have that $L_6, L_8, L_7 \rightarrow 0$.

$$\begin{aligned}
L_0 &\rightarrow \theta_2 \\
L_1 &\rightarrow \eta^2 \theta_4 \\
L_2 &= \eta \theta_3 \\
L_3 &\rightarrow \gamma_1^2 \mathbb{E}_{X \sim \mu_{\psi_1}} \left[\frac{1}{\gamma_1^2 X + \gamma_2^2} \right] = \theta_1 \\
L_4 &\rightarrow \gamma_1^2 \eta^2 \theta_4 \cdot \psi_1 \mathbb{E}_{X \sim \mu_{\psi_1}} \left[\frac{X}{\gamma_1^2 X + \gamma_2^2} \right] = \eta^2 \theta_2 \theta_4 \\
L_5 &\rightarrow \gamma_1^2 \eta \theta_3 \cdot \psi_1 \mathbb{E}_{X \sim \mu_{\psi_1}} \left[\frac{X}{\gamma_1^2 X + \gamma_2^2} \right] = \eta \theta_2 \theta_3 \\
L_6, L_7, L_8 &\rightarrow 0 \\
D &\rightarrow L_3(L_4 - L_1) - 1 \rightarrow \eta^2 \theta_1 (\theta_2 - 1) \theta_4 - 1
\end{aligned}$$

To sum up, we have

$$\begin{aligned}
\lim_{d \rightarrow \infty} \tau_{d,\eta} &= 1 - \theta_2 - \frac{\eta^2 \theta_1 \theta_3^2 (\eta^2 \theta_1 (\theta_2 - 1) \theta_4 - 1)}{\eta^2 \theta_1 (\theta_2 - 1) \theta_4 - 1} \\
&\quad + \frac{\eta^4 \theta_1^2 (\theta_2 - 1) \theta_3^2 \theta_4}{\eta^2 \theta_1 (\theta_2 - 1) \theta_4 - 1} \\
&\quad + \frac{\theta_1 \theta_2^2 \theta_3^2}{\eta^2 \theta_1 (\theta_2 - 1) \theta_4 - 1} \\
&\quad - 2 \frac{\eta^2 \theta_1 \theta_2 \theta_3^2}{\eta^2 \theta_1 (\theta_2 - 1) \theta_4 - 1} \\
&= 1 - \theta_2 - \frac{\eta^2 \theta_1 (1 - \theta_2)^2 \theta_3^2}{1 + \eta^2 \theta_1 (1 - \theta_2) \theta_4}.
\end{aligned}$$

This completes the proof for the first part of [Theorem C.4](#).

Step 5: Analysis for prediction accuracy. Recall from [Setting C.2](#) the definition of prediction accuracy of the network after a gradient step is $\Pr_{(\mathbf{x}, y) \sim \mathcal{D}_F(\beta_*)} [y \mathbf{a}^\top \sigma(W_1 \mathbf{x}) \geq 0]$. By Gaussian equivalence and [Proposition C.5](#), we have that the following.

$$\begin{aligned}
&\text{Acc}_{P_{\text{train}, d, N}}(\psi_1, \psi_2, \eta) \\
&= \Pr_{\substack{(\mathbf{x}, y) \sim \mathcal{D}_F(\beta_*) \\ \mathbf{a}, W_1}} [y \mathbf{a}^\top \sigma(W_1 \mathbf{x}) \geq 0].
\end{aligned}$$

By [Proposition C.5](#), we can further approximate the equation as follows.

$$= \Pr_{\substack{(\mathbf{x}, y) \sim \mathcal{D}_F(\beta_*) \\ \mathbf{a}, W_0, \mathbf{u}}} [y \mathbf{a}^\top \sigma((W_0 + \mathbf{a} \mathbf{u}^\top) \mathbf{x}) \geq 0] + o(1).$$

By Gaussian equivalence, we can further approximate the equation as follows.

$$= \Pr_{\substack{(\mathbf{x}, y) \sim \mathcal{D}_F(\beta_*) \\ \mathbf{a}, W_0, W_*, \mathbf{u}}} [y \mathbf{a}^\top (\gamma_1 (W_0 + \mathbf{a} \mathbf{u}^\top) + \gamma_* W_*) \mathbf{x} \geq 0] + o(1)$$

where $W_* \in \mathbb{R}^{N \times d}$ and $([W_*]_{kj} \sim \mathcal{N}(0, 1/N))$ for each $k \in [N], j \in [d]$. Note that as \mathbf{a}, W_0, W_* are independent, we can further simplify the equation as follows.

$$= \Pr_{\substack{(\mathbf{x}, y) \sim \mathcal{D}_F(\beta_*) \\ \mathbf{a}, W'_*, \mathbf{u}}} [y \gamma_1 \mathbf{u}^\top \mathbf{x} + \sqrt{\gamma_1^2 + \gamma_*^2} \cdot y \mathbf{a}^\top W'_* \mathbf{x} + o(1) \geq 0] + o(1)$$

where $W'_* \in \mathbb{R}^{N \times d}$ and $([W'_*]_{kj} \sim \mathcal{N}(0, 1/N))$ for each $k \in [N], j \in [d]$. Note that as \mathbf{a}, W'_* are independent, we can further simplify the equation as follows.

$$= \Pr_{\substack{(\mathbf{x}, y) \sim \mathcal{D}_F(\beta_*) \\ Z \sim \mathcal{N}(0, 1)}} \left[\eta \gamma_1^2 \mathbb{E}_{(\mathbf{x}', y') \sim \mathcal{D}_F(\beta_*)} [y y' \mathbf{x}'^\top \mathbf{x}] + \sqrt{\gamma_1^2 + \gamma_*^2} \cdot Z + o(1) \geq 0 \right] + o(1).$$

Note that by decomposing \mathbf{x} and \mathbf{x}' to direction that's parallel to β_* and orthogonal to β_* , we can further simplify the equation as follows.

$$\begin{aligned}
&= \Pr_{\substack{(G,Y) \sim \mathcal{D}_F \\ Z, Z' \sim \mathcal{N}(0,1)}} \left[\eta \gamma_1^2 \left(\mathbb{E}_{(G',Y') \sim \mathcal{D}_F} [YY'GG'] + \sqrt{1/\psi_2} Z' \right) + \sqrt{\gamma_1^2 + \gamma_*^2} \cdot Z + o(1) \geq 0 \right] + o(1) \\
&= \Pr_{\substack{(G,Y) \sim \mathcal{D}_F \\ Z \sim \mathcal{N}(0,1)}} \left[\eta \gamma_1^2 \theta_3 YG + \sqrt{\frac{\eta^2 \gamma_1^4}{\psi_2} + \gamma_1^2 + \gamma_*^2} \cdot Z + o(1) \geq 0 \right] + o(1) \\
&= \mathbb{E}_{(G,Y) \sim \mathcal{D}_F} \left[\Phi \left(\frac{\eta \gamma_1^2 \theta_3}{\sqrt{\frac{\eta^2 \gamma_1^4}{\psi_2} + \gamma_1^2 + \gamma_*^2}} YG \right) \right] + o(1).
\end{aligned}$$

Note that when fixing ψ_1, ψ_2 and non-trivial F , both capacity formula and prediction accuracy formula are increasing and invertible with respect to η . As a consequence, the two quantities are also analytically connected by an increasing and invertible function. This completes the proof for the second part of [Theorem C.4](#). We also provide numeric checks for the formulas in [Figure 13](#).

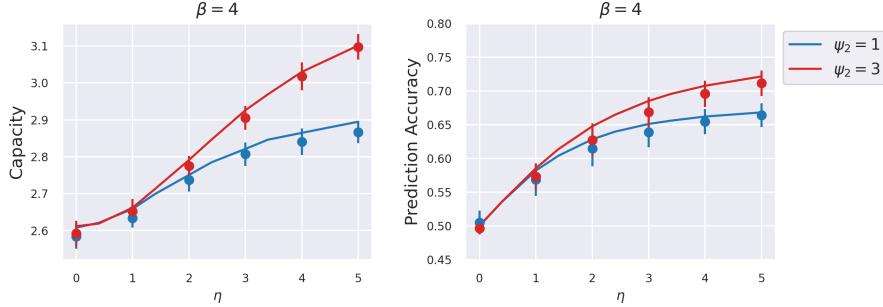


Figure 13: Numerical checks for the formulas in [Theorem C.4](#). We run the simulation with $d = 2000$, $\psi_1 = 1$, ReLU activation, and label function $f(x) = \frac{1}{1+e^{-4x}}$ for 50 repetitions. Left: numerical checks for the capacity formula. Right: numerical checks for the prediction accuracy formula.

D 2-Layer Non-linear Neural Networks

In this paper, we use 2-layer non-linear neural networks and Gaussian mixture models (for input data generation) as a convenient experimental setup to systematically explore different regimes in feature learning. Moreover, given its medium level of complexity, it might be possible to have an analytical characterization of our numerical findings, and we leave it as an interesting future direction.

D.1 Experimental setup

D.1.1 Synthetic data generation

We focus on point manifold, which consists of data points associated with the same label. As discussed in the previous section, we are particularly interested in the effective radius, dimension, center alignment, axes alignment, and center-axes alignment of the representation manifolds. Therefore, we consider a synthetic model to generate training and test data with relevant geometric

interpretations. Namely, construct $P \in \mathbb{N}$ synthetic data manifolds with radius $R \in \mathbb{R}_+$, intrinsic dimension $D \in \mathbb{N}$, size $M \in \mathbb{N}$. The manifold layouts are further determined by center correlation strength $\rho_C \in [0, 1)$, axes correlation strength $\rho_A \in [0, 1)$, and center-axes correlation strength $\psi \in [0, 1)$, all of which we would detail in the following subsections.

Isotropic spherical manifolds. First, we consider the simplest case: manifolds with isotropic Gaussian center distribution and axes distribution with no correlations. This is the scenario considered in [Section 3](#) and [Section 4](#).

Let $d \in \mathbb{N}$ be the dimension of the data. We consider P point manifolds $\{\mathcal{M}_i\}_{i \in [P]}$ with manifold size $M \in \mathbb{N}$ and radius R that lies in a subspace of dimension D . Each manifold is defined as

$$\mathcal{M}_i = \{\mathbf{u}_0 + R \cdot \sum_{j=1}^D s_j^k \mathbf{u}_j + \epsilon \mathbf{v}_k\}_{k \in [M]}$$

where the axes $\mathbf{u}_j \sim N(0, I_d/d)$, the coordinates $s_j^k \sim N(0, 1)$, the noise vectors $\mathbf{v}_k \sim N(0, I_d/d)$, and $\epsilon = 10^{-2}$. The pre-scaled points in the manifolds $\{\sum_{j=1}^D s_j^k \mathbf{u}_j\}_{k \in [M]}$ are well-normalized to unit norm.

Test manifolds share the same model except that the noise vectors \mathbf{v}_j are sampled again in the same distribution.

Isotropic Gaussian manifolds. In certain experiments, we drop in the intrinsic dimension D and directly consider manifolds defined as

$$\mathcal{M}_i = \{\mathbf{u}_0 + R \cdot \mathbf{v}_k\}_{k \in [M]}$$

where the noise vectors are $\mathbf{v}_k \sim N(0, I_d/d)$. Test manifolds share the same model except that the noise vectors \mathbf{v}_k are sampled again in the same distribution.

Correlated spherical manifolds. To generate correlated manifolds, we consider an autoregressive model described by the covariance matrix $C = (\rho^{|i-j|})_{i,j} \in \mathbb{R}^{P \times P}$, where $\rho \in [0, 1)$ is either the center correlation strength ρ_C or axes correlation strength ρ_A . The center covariance C_C is then mixed into the isotropic manifold centers $\{\mathbf{u}_0^j \sim N(0, I_d/d)\}_{j \in [M]}$. The axes covariance matrices C_A^i is mixed into the isotropic axes $\{\mathbf{u}_i^j \sim N(0, I_d/d)\}_{j \in [M]}$ for each $i = 1, 2, \dots, D$ respectively. The mixing is performed through multiplying the column matrix M_C or $M_A^j \in \mathbb{R}^{P \times d}$ of centers or each axes with the Cholesky decomposition of C_C or C_A^i . To incorporate center-axes correlation, we scale each center vector \mathbf{u}_0 by a factor of $(1 + \psi \cdot q)$ where $q \sim N(0, 1)$.

Labels. For P manifolds with manifold size M , the P labels are randomly sampled from a uniform distribution on $\{\pm 1\}$. Each label is associated with M data points in the individual manifold. When learning with binary cross entropy, the labels are reassigned as $\{0, 1\}$ during loss and gradient computation.

D.1.2 2-Layer neural network architecture

The model architecture we consider is similar to the architecture mentioned in [Appendix C](#).

Let $d \in \mathbb{N}$ be the input data dimension, $N \in \mathbb{N}$ be the number of hidden neurons, $K \in \mathbb{N}$ be the number of linear readouts, $\alpha \in \mathbb{R}_+$ be the scaling factor of the readout weights.

Let $W = W_0 \in \mathbb{R}^{N \times d}$ be the initial weight matrix of a fully connected 2-layer neural network. Let $\{a_0^i\}_{i \in [K]}$ be a list of initial readout weights where $a_0^i \in \mathbb{R}^N$. Let $\sigma(\cdot) : \mathbb{R} \rightarrow \mathbb{R}$ be a non-linear activation function, e.g. ReLU or tanh.

The feature of an input vector is defined as $\phi(\mathbf{x}) = \sigma(W\mathbf{x})$. The 2-layer neural network parameterized by W and a^i is defined as

$$f(W, a^i; \mathbf{x}) = \frac{\alpha}{\sqrt{N}} \mathbf{a}^\top \phi(\mathbf{x})$$

where the label prediction for data point \mathbf{x} is $\text{sgn}(f(\mathbf{x}))$ when learning with the mean squared error loss function. When learning with binary cross entropy loss function, we use $\{0, 1\}$ as labels and $\varsigma(f(\mathbf{x}))$ as prediction instead, where ς is the standard sigmoid function.

D.1.3 Learning rule

Loss function and gradient update. Let $\eta \in \mathbb{R}_+$ be the learning rate of the weight matrix, $c \in \mathbb{R}_+$ be the scaling factor of the readout learning rate, and let $\{(\mathbf{x}_i, y_i)\}_{i \in [PM]}$ be the collection of training data, where P is the number of manifolds and M is the manifold size.

We consider gradient descent over the loss function

$$\mathbb{L}(f) = \frac{1}{\alpha^2} \frac{1}{PM} \sum_{i \in [PM]} \ell(f(\mathbf{x}_i), y_i)$$

where $\ell : \mathbb{R} \times \{\pm 1\} \rightarrow \mathbb{R}$ is either the mean squared error (MSE)

$$\ell_{MSE}(z, y) = \frac{1}{2}(z - y)^2$$

or $l : \mathbb{R} \times \{0, 1\} \rightarrow \mathbb{R}$ is the binary cross entropy (BCE)

$$\ell_{BCE}(z, y) = y \cdot \log(1 + e^{-z}) + (1 - y) \cdot \log(1 + e^z)$$

Mean squared error. For the weight matrix, the gradient update with learning rate $\eta > 0$ is $W_{t+1} = W_t + \eta G_t$ where

$$G_t = \frac{1}{\alpha^2} \frac{1}{PM} \sum_{i \in [PM]} \frac{1}{K} \sum_{j \in [K]} \left[\left(y_i - \frac{\alpha}{\sqrt{N}} \mathbf{a}_t^j \top \sigma(W_t \mathbf{x}_i) \right) \frac{\alpha}{\sqrt{N}} \mathbf{a}_t^j \odot \sigma'(W_t \mathbf{x}_i) \right] \mathbf{x}_i^\top$$

and $\sigma'(\cdot)$ denotes the first order derivative of $\sigma(\cdot)$. For each linear readout, the gradient update is $a_{t+1} = a_t + c\eta g_t$ where

$$g_t = \frac{1}{\alpha^2} \frac{1}{PM} \sum_{i \in [PM]} \left[y_i - \frac{\alpha}{\sqrt{N}} \mathbf{a}_t^\top \sigma(W_t \mathbf{x}_i) \right] \frac{\alpha}{\sqrt{N}} \sigma(W_t \mathbf{x}_i)$$

Note that the α^{-2} multiplier on the loss function to ensure common convergence time when $\alpha \rightarrow \infty$ as mentioned in (Geiger et al., 2020).

Binary cross entropy. For the weight matrix, the gradient update with learning rate $\eta > 0$ is $W_{t+1} = W_t + \eta G_t$ where

$$G_t = \frac{1}{\alpha^2} \frac{1}{PM} \sum_{i \in [PM]} \frac{1}{K} \sum_{j \in [K]} \left[(y_i - \varsigma[\frac{\alpha}{\sqrt{N}} \mathbf{a}_t^{j\top} \sigma(W_t \mathbf{x}_i)]) \frac{\alpha}{\sqrt{N}} \mathbf{a}_t^j \odot \sigma'(W_t \mathbf{x}_i) \right] \mathbf{x}_i^\top$$

where ς denotes the standard sigmoid function and σ denotes the activation function. For each linear readout, the gradient update is $a_{t+1} = a_t + c\eta g_t$ where

$$g_t = \frac{1}{\alpha^2} \frac{1}{PM} \sum_{i \in [PM]} \left[y_i - \varsigma[\frac{\alpha}{\sqrt{N}} \mathbf{a}_t^\top \sigma(W_t \mathbf{x}_i)] \right] \frac{\alpha}{\sqrt{N}} \sigma(W_t \mathbf{x}_i)$$

If not otherwise noted, we conduct experiments with the MSE loss function and ReLU activation function by default.

A Note on Learning rate. We define $\bar{\eta} = \eta\alpha^{-1}$ as the normalized effective learning rate. During training, We implicitly scale the learning rate η by a factor of \sqrt{N} in the experiments to enter the rich regime as mentioned in (Ba et al., 2022).

D.1.4 Training

For each 2-layer neural network experiment conducted in the paper, forty random seeds are chosen from 0 to 39000 with an interval of 1000 to train forty models in parallel for 10^5 epochs. All training are conducted on the Flatiron Institute high performance computing clusters.

D.1.5 Feature extraction

During analysis, fifty epochs are sampled uniformly in log-scale. For each model at checkpoint epoch t , we extract total P size M manifold representations $\{\Phi_t(\mathbf{x}_i)\}_{i \in [PM]}$ associated with labels $\{y_i\}_{i \in [PM]}$. We perform conventional analysis and manifold capacity analysis described in Appendix A and Appendix B respectively. We will present more details in the following experiment sections.

D.2 Capacity is a robust measure of feature learning across architecture, data, and learning rule variations

The purpose of this section is to support Section 3 by showcasing that capacity is able to quantify feature learning even when model architecture, data distribution, and learning rule varies.

D.2.1 Feature analysis methods

Here, we briefly present the conventional feature analysis methods and capacity analysis method and how they are computed in the experimental setup.

Representation level analysis. Activation stability is a representation level metric that intuitively captures how much neurons are activated in hidden units. Formally, we define it as

$$\frac{\sum_{i=1}^{PM} \sum_{j=1}^N \mathbf{1}_{>0}(\phi_j(\mathbf{x}_i))}{PMN}$$

Another conventional method to disentangle feature learning at representation level is tracking the norm of deviation from initial weights (Jacot et al., 2020)

$$\frac{\|W_t - W_0\|}{\|W_0\|}$$

On the other hand, the cosine similarity (Liu et al., 2024) can be used to study alignment at representation level

$$\frac{\Phi_t \Phi_0}{\|\Phi_t\| \|\Phi_0\|}$$

where $(\Phi_t)_{ij} = \phi_t(\mathbf{x}_i) \cdot \phi_t(\mathbf{x}_j) \in \mathbb{R}^{PM \times PM}$ is the gram matrix of features over the test data.

Kernel methods. The kernel methods for quantifying feature learning involves computing the Neural Tangent Kernel (NTK) (Jacot et al., 2020) for each pair of test data points:

$$\Theta_t(\mathbf{x}_1, \mathbf{x}_2) = \nabla_{w_t} f(\mathbf{x}_1) \cdot \nabla_w f(\mathbf{x}_2)$$

where $\nabla_{w_t} f$ denotes the total gradient of the neural network at epoch t with respect to the hidden weights W_t and readout weights $\{a_t^j\}$. Note that we scale the readout contribution to the total gradient by the readout learning rate factor $c \in \mathbb{R}_+$ aforementioned. Hence,

$$\nabla_w f(\mathbf{x}) = \nabla_{W_t} f(\mathbf{x}) + \frac{1}{K} \sum_{j=1}^K \nabla_{a_t^j} f(\mathbf{x})$$

After obtaining the gram matrix $\Theta_t = \Theta_t(\mathbf{x}_i, \mathbf{x}_j)_{ij} \in \mathbb{R}^{PM \times PM}$ from the test data, we can compute the *NTK change* defined as

$$\frac{\|\Theta_t - \Theta_0\|}{\|\Theta_0\|}$$

which can be interpreted as the relative deviation of the the kernel from initialization in the Frobenius norm metric. Conventionally studied, NTK change disentangles lazy and feature learning, as detailed in (Jacot et al., 2020). We present NTK change in Section 3 Figure 4 to compare it with capacity as the metric to track feature learning.

The *kernel alignment* can be similarly defined as the cosine similarity of initial and current NTK gram matrices:

$$\frac{\Theta_t \Theta_0}{\|\Theta_t\| \|\Theta_0\|}$$

which can be interpreted as the relative deviation of the kernel from initialization in terms of alignment. Kernel alignment is also studied in (Liu et al., 2024) to disentangle lazy and feature learning.

The *centered kernel alignment* (Kornblith et al., 2019) is another approximation method to study kernel evolution when the gram matrices is large:

$$\frac{HSIC(\Theta_t, \Theta_0)}{\sqrt{HSIC(\Theta_t, \Theta_t) HSIC(\Theta_0, \Theta_0)}}$$

where

$$HSIC = \frac{\text{Tr}(\Theta_t L \Theta_0 L)}{(n-1)^2}$$

These kernel metrics can be readily computed from the trained models and extracted features.

Capacity and effective geometry. For more details on data-driven manifold capacity analysis, please refer to [Appendix B](#).

Setup of Figure 4a. In [Figure 4a](#), we showcase that the degree of feature learning is controlled by the effective learning rate $\bar{\eta}$ with the following standard setup:

- Data: Isotropic Gaussian manifolds with $R = 0.5, M = 15$.
- Model: We set $\sigma = \text{ReLU}, N = 1500, d = 1000, P = 100, K = 1$.
- Learning rule: We set $\ell = \ell_{MSE}, \eta = 50, c = 0$ and

$$\alpha = 10/128, 10/112, 10/96, 10/80, 10/64, 10/16, 10/4, 10/1$$

so that the normalized effective learning rates are

$$\bar{\eta} = 128, 112, 96, 80, 64, 16, 4, 1$$

which is computed by $\bar{\eta} = \frac{\eta\alpha^{-1}}{5}$ where the division by 5 normalizes the smallest $\eta\alpha^{-1}$ to be 1.

- Training: We trained the models for 100000 epochs with 40 repetitions per parameter combination.
- Plotting: We use sample mean and 95% confidence interval for each data point.

D.3 Effective geometry reveals distinct learning dynamics

D.3.1 Learning strategies

Compression strategy setup In [Figure 5b](#) where the networks performs the compression strategy, we use a difficult-task setup with higher data manifold radius and more readout tasks:

- Data: Isotropic spherical manifolds with $R = 1.0, D = 8, M = 15$.
- Model: We set $\sigma = \text{ReLU}, N = 300, d = 200, P = 20, K = 27$.
- Learning rule: we set $\ell = \ell_{MSE}, \alpha = 1, c = 0$ and

$$\eta = 1, 5, 10, 20, 30, 40, 50, 60, 70, 80, 90, 100, 110, 120, 130, 140, 150$$

so that the normalized effective learning rates are

$$\bar{\eta} = 1, 5, 10, 20, 30, 40, 50, 60, 70, 80, 90, 100, 110, 120, 130, 140, 150.$$

- Training: We trained the models for 100000 epochs with 40 repetitions per parameter combination.
- Plotting: We use sample mean for each data point.

Flattening strategy setup. In Figure 5b where the networks performs the flattening strategy, we use an easy-task setup with smaller data manifold radius and very few readout tasks:

- Data: Isotropic spherical manifolds with $R = 0.5, D = 8, M = 15$.
- Model: We set $\sigma = \text{ReLU}, N = 300, d = 200, P = 20, K = 3$.
- Learning rule: we set $\ell = \ell_{MSE}, \alpha = 1, c = 0$ and

$$\eta = 80, 90, 100, 110, 120, 130, 140, 150, 160, 170$$

so that the normalized effective learning rates are

$$\bar{\eta} = 80, 90, 100, 110, 120, 130, 140, 150, 160, 170.$$

- Training: We trained the models for 100000 epochs with 40 repetitions per parameter combination.
- Plotting: We use sample mean for each data point.

Contour plot of learning strategies. In Figure 5b and c, we use contour plots to visualize the different learning strategies adopted by the network. We use Equation 34 in (Chung et al., 2018) to approximate capacity using effective radius and dimension:

$$\alpha = \frac{1 + \left(\frac{1}{R_M^2}\right)}{D_M}$$

The scatter points with the same color correspond to a model trained with the same normalized effective learning rate $\bar{\eta}$ over different epochs.

D.3.2 Learning stages

Setup. In Figure 5a, we adopt a setup with moderate radius and number of readout tasks that shows clean learning stages:

- Data: Isotropic spherical manifolds with $R = 1, D = 8, M = 15$.
- Model: We set $\sigma = \text{ReLU}, N = 300, d = 200, P = 20, K = 5$.
- Learning rule: we set $\ell = \ell_{MSE}, \eta = 10, \alpha = 1, c = 0$ so that the normalized effective learning rate is $\bar{\eta} = 10$.
- Training: We trained the models for 100000 epochs with 40 repetitions per parameter combination.
- Plotting: We use sample mean for each data point.

E Deep Neural Networks

E.1 Experimental setup

In this section, we provide detailed information about the experimental setup for deep neural networks, including model architectures, datasets, training procedure, and manifold capacity measurements.

E.1.1 Models

We use the VGG-11 models (Simonyan and Zisserman, 2014) for experimental results in the main paper. We also repeat these experiments on ResNet-18 (He et al., 2016). The specific implementation follows a similar setting in (Chizat et al., 2019) and is adapted from <https://github.com/edouardoyallon/la>

Output rescaling . As previously studied in (Chizat et al., 2019), multiplying the model outputs by a large scaling factor β can induce lazy learning (we use the notation β instead of α in (Chizat et al., 2019) to avoid confusion with the notation α as capacity in Equation A.1). In this section, we use the inverse scaling factor β^{-1} as the parameter to control the degree of feature learning. We define the *normalized effective learning rate* $\bar{\eta} = \beta^{-1}$. We also note several adjustments to the common training framework to adapt to using the inverse scaling factor β^{-1} as the parameter to control the degree of feature learning.

- Rescaled loss function: To adjust for using the scaling factor β , we use the rescaled loss function $L_\beta = \frac{L}{\beta^2}$ with L denotes the loss function to accommodate for the time parameterization of the loss dynamic for large β as previously indicated in (Chizat et al., 2019) and (Geiger et al., 2020).
- Model’s initial outputs as 0: As mentioned in (Chizat et al., 2019), for the scaling factor β to be able to control the rate of feature learning, the model output as initialization $f(W_0)$ must be equal 0. To ensure this condition, we set $f(W_t) = h(W_t) - h(W_0)$ with W_t be the model’s weight at training step t , h be the output of the network, and f be the final adjusted network output.

Number of repetitions. All model measurements (train accuracy, test accuracy, activation stability, etc.) are reported as the mean of 5 independently trained model (with different random seeds). The error bar indicates the bootstrapped 95% confidence interval calculated using `seaborn.lineplot(errorbar='ci', 95)`.

E.1.2 Dataset

In this section, we list detailed information about the dataset used in the paper.

CIFAR-10. The CIFAR-10 dataset (Krizhevsky and Hinton, 2009) consists of 60000 32x32 colour images in 10 classes, with 6000 images per class. There are 50000 training images and 10000 test images.

CIFAR-100. The CIFAR-100 dataset (Krizhevsky and Hinton, 2009) is similar to CIFAR-10, except that it has 100 classes containing 600 images each. There are 500 training images and 100 testing images per class. Note that the images in CIFAR-10 and CIFAR-100 are mutually exclusive.

CIFAR-10C. The CIFAR-10C dataset (Hendrycks and Dietterich, 2018) includes images from the CIFAR-10 evaluation set with common corruptions such as Gaussian noise, fog, motion blur, etc. The dataset has 15 different common corruption types, and 5 different severity levels for each corruption type.

E.1.3 Training procedure

- Loss function: We follow the theoretical results and practice used in (Chizat et al., 2019) to use mean-squared error loss to train all DNNs mentioned in the paper.
- Optimizer: We use Stochastic Gradient Descent with momentum (implemented as `torch.optim.SGD(momentum)` to train the models.
- Data augmentation: We apply the following data augmentation during training: `RandomCrop(32, padding=4)`, `RandomHorizontalFlip`.
- Learning rate and learning schedule: We follow the practice in (Chizat et al., 2019) and set initial learning rate $\eta_0 = 1.0$ for VGG-11 and $\eta_0 = 0.2$ for ResNet-18. The learning rate schedule is defined as $\eta_t = \frac{\eta_0}{1 + \frac{1}{3}t}$.
- Initialization: We follow the practice in (Chizat et al., 2019) to initialize the model’s weight using Xavier initialization (Glorot and Bengio, 2010) and the bias to be 0.
- Batch size: We use batch size of 128 during training and batch size of 100 during evaluation.

E.1.4 Manifold capacity measurements

In this section, we provide detailed information about how we define object manifolds from the model’s representations and measure the manifold capacity and geometric properties (Chung et al., 2018).

- Features extraction: For each image, we extract the object representation from the last linear layer (dimension 512) before the classification layer (dimension 10).
- Number of manifolds: We use 10 object manifolds for each measurement.
- Number of points per manifold: For each object manifold, we randomly sample 50 images from the interested class.
- Number of repetitions: Every capacity and geometry measurement is repeated 10 times per model instance (50 times if we have 5 model repetitions) and we report the mean and the error bar as the bootstrapped 95% confidence interval calculated using `seaborn.lineplot(errorbar=('ci', 95))`.

E.2 Capacity quantifies the degree of feature learning in deep neural networks

Capacity and manifold geometry for VGG-11 models. In Figure 4, we show manifold capacity along with other common metrics used to identify feature learning such as train accuracy, test accuracy, relative weight norm change, and activation stability. In this section, we provide other manifold geometric measurements along with manifold capacity in Figure 14.

Capacity quantifies the degree of feature learning in ResNet-18 models. In section Section 3, we show that manifold capacity can capture the degree of feature learning in DNNs, specifically in VGG models. In this section, we empirically show this statement can also be extended to other model architectures, specifically ResNets, in Figure 15.

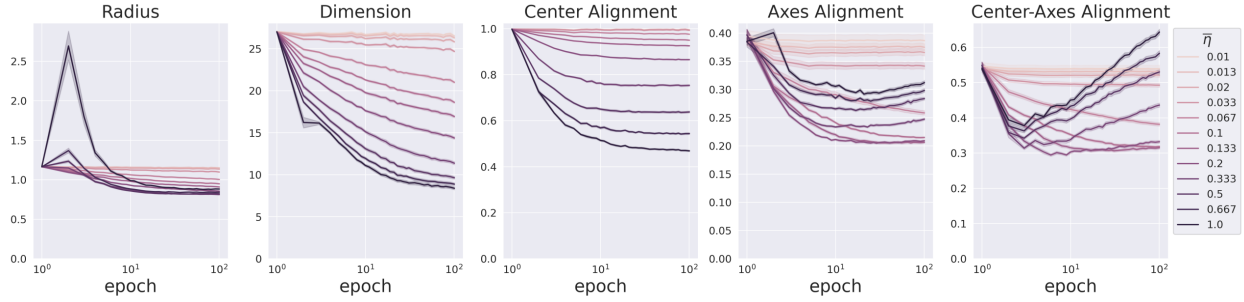
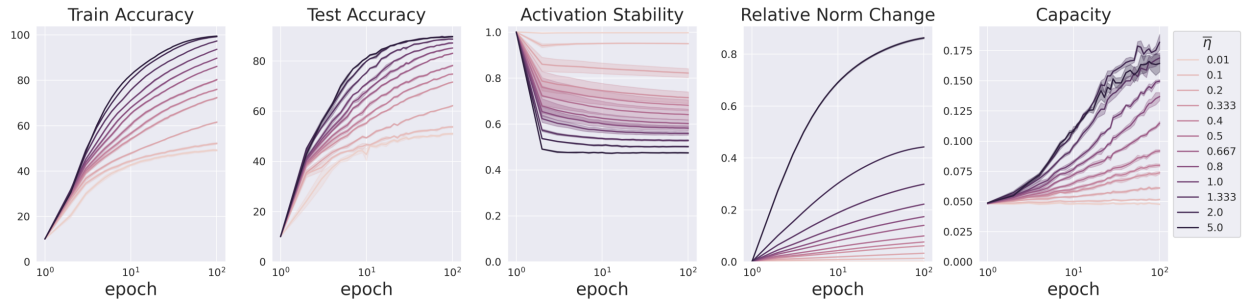
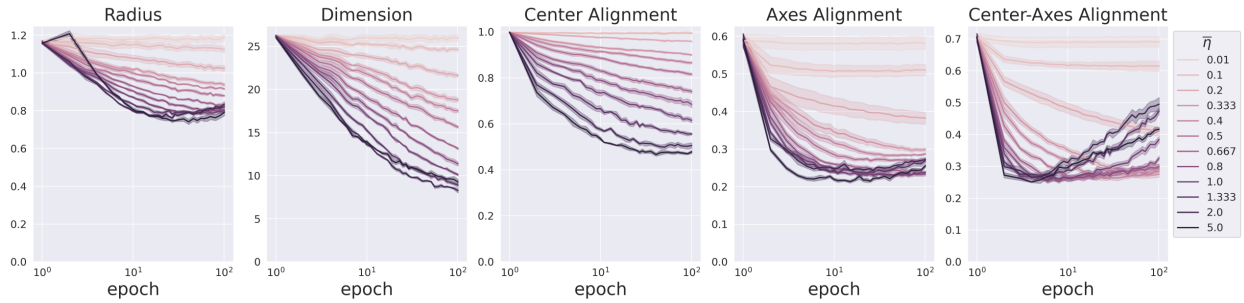


Figure 14: Manifold capacity and geometry for VGG-11 models trained with different $\bar{\eta}$



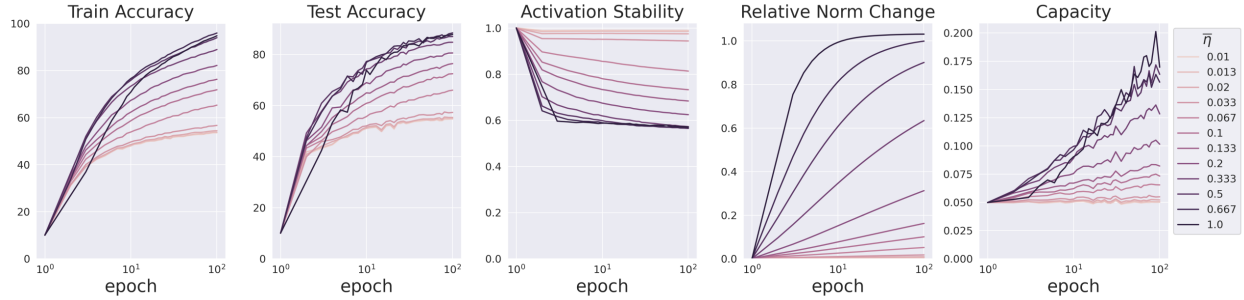
(a) Manifold capacity captures the degree of feature learning in ResNet-18



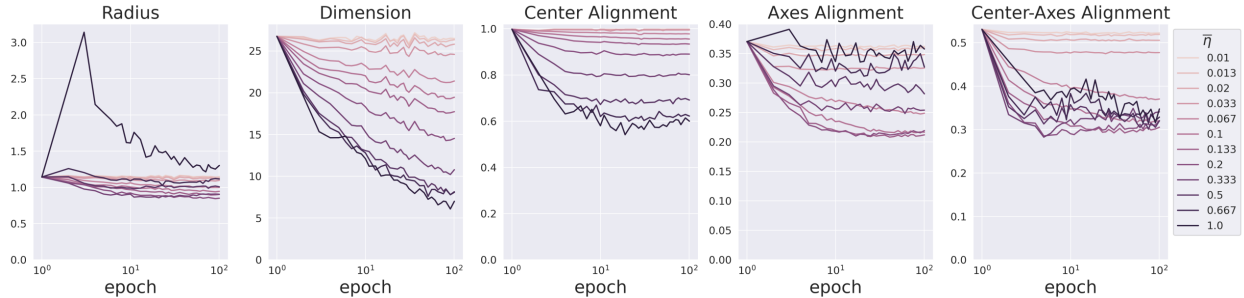
(b) Manifold geometry for ResNet-18 models trained with different $\bar{\eta}$

Figure 15: Manifold capacity and geometry of ResNet-18 models trained with different scale factor.

Capacity quantifies the degree of feature learning in VGG-11 models trained with weight regularizer. While most theoretical work in the lazy vs rich learning literature are formulated with vanilla mean squared error (MSE) loss (Jacot et al., 2020) (Chizat et al., 2019), in practice, MSE with weight regularizer (or weight decay) is used widely to prevent over-fitting and improve model generalization. In Figure 16, we explore the effect of weight decay to feature learning and demonstrate empirically that capacity can still quantify the degree of feature learning in models trained with L2-regularizer. We implemented L2-regularizer by setting `torch.optim.SGD(weight_decay=0.0002)`. We leave further study about the impact between the magnitude of weight regularizer and effective learning rate (and/or scaling factor) to the degree of feature learning as a potential future direction.



(a) Manifold capacity captures the degree of feature learning in VGG-11 models trained with L2-regularizer



(b) Manifold geometry for VGG-11 models with L2-regularizer trained with different $\bar{\eta}$

Figure 16: Manifold capacity and geometry of VGG-11 models with L2-regularizer trained with different scale factor.

E.3 Manifold capacity and manifold geometry delineate learning stages in deep neural networks

In section Section 4.2, we have demonstrated the use of effective manifold geometry to uncover hidden learning stages in 2-layer neural networks. In this section, we showed that using similar technique, we can also discover geometric learning stages in deep neural networks as well.

Experiment setup We used similar setup mentioned in Section E.1. In this section, to give a higher resolution into the learning dynamic, we extracted the model checkpoint at each training step (after each training batch, with `batch_size=100`) instead of each training epoch (after a whole train dataset iteration).

E.4 Feature learning and downstream task: out-of-distribution generalization

In this section, we measure the performance of the models trained with different degree of feature learning (quantified by effective learning rate $\bar{\eta}$) on the downstream tasks for OOD using CIFAR-100, a dataset with no overlap with CIFAR-10, the dataset used to train the model.

E.4.1 Experimental setup

We use linear probe (Alain and Bengio, 2016) on representation from the last linear layer (dimension 512) to measure the performance of models trained on CIFAR-10 on the out-of-distribution dataset, CIFAR-100. Linear probes are linear classifiers trained on top of the representation to probe how much information the representations encode about a particular task or characteristic. This

approach has been used widely in different fields including natural language processing (Belinkov et al., 2017) and computer vision (Raghu et al., 2021).

Here we provide detailed information about how we construct the linear probes.

Optimizer. We use *Adam* optimizer with initial learning rate $\eta_0 = 0.1$ and learning rate schedule is defined as $\eta_t = \frac{\eta_0}{1+\frac{1}{3}t}$. Other parameters are default *Pytorch* parameters.

Number of epochs. The linear probe is trained for 50 epochs, unless it is stopped early, as described by the early stop method below.

Early stop. During training, if the validation loss is greater than the minimum validation loss so far for more than $N_{patience}$ epoch, then training is stopped. We set $N_{patience} = 3$.

E.4.2 OOD performance for ResNet-18

In Section 5.2, we demonstrate how capacity and effective manifold geometry can be used to characterize the OOD performance of VGG-11 models trained with different effective learning rate $\bar{\eta}$. In this section, we show OOD performance and effective geometry of ResNet-18 models trained with different effective learning rate $\bar{\eta}$ in Figure 17. Interestingly, unlike VGG-11, for ResNet-18, the failure of models in the ultra-rich regime is characterized by the expansion of manifold dimension, not manifold radius.

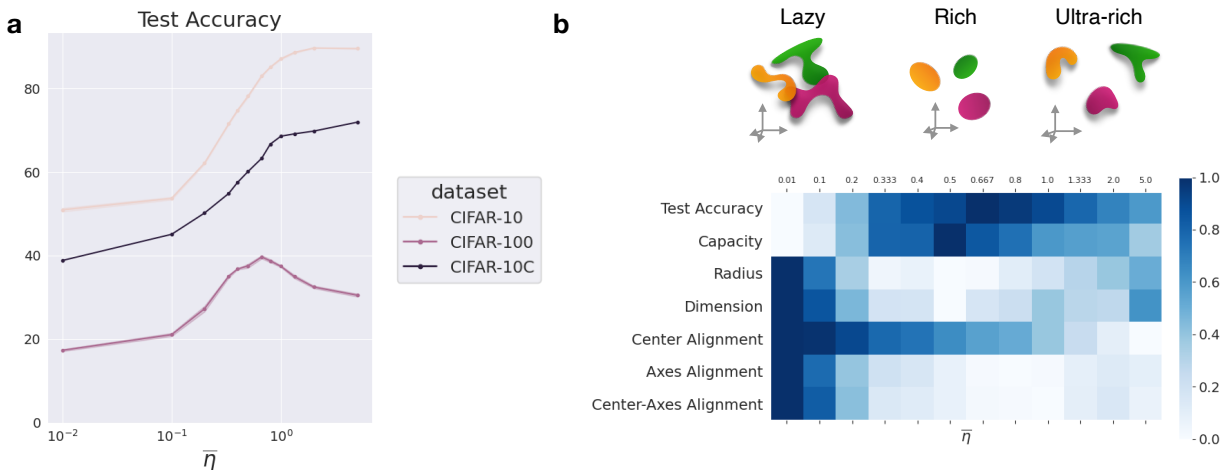


Figure 17: OOD performance and effective geometric measure of ResNet-18 models trained with different scale factor.

F Recurrent Neural Networks

F.1 Experimental Setup

In this section, we provide detailed information about the experimental setup for recurrent neural network in 5.1, including model architectures, datasets, training procedure, and manifold capacity measurements.

F.1.1 Dataset

We used the package `neurogym` (Molano-Mazon et al., 2022) to simulate common cognitive tasks. In this paper, we trained recurrent neural networks to perform the following cognitive tasks: perceptual decision making, context decision making, and delay match sample. We followed the task configuration used in (Liu et al., 2024). We list detailed information of task configuration and descriptions below.

Perceptual decision making (Britten et al., 1992) (documentation page)

- Task description: In each trial, given two noisy stimulus, the agent needs to integrate the stimulus over time to determine which stimuli has stronger signal.
- Task configuration: We set up the task using the following parameters: `{timing: {fixation: 0, stimulus: 700, delay: 0, decision: 100}, dt: 100, seq_len: 8}`

Context decision making (Mante et al., 2013) (documentation page)

- Task description: In each trial, given two noisy stimulus, each has two modalities, the agent needs to integrate the stimulus in one specific modal while ignoring the other modal. The interested modal is given by the context.
- Task configuration: We set up the task using the following parameters: `{timing: {fixation: 0, stimulus: 200, delay: 500, decision: 100}, dt: 100, seq_len: 8}`

Delay match sample (Miller et al., 1996) (documentation page)

- Task description: In each trial, a sample stimulus is shown during the sample period, which followed by a delay period. Afterwards, the test stimulus is shown. The agent needs to determine whether the sample and the test stimuli are matched.
- Task configuration: We set up the task using the following parameters: `{timing: {fixation: 0, sample: 100, delay: 500, test: 100, decision: 100}, dt: 100, seq_len: 8}`

F.1.2 Models

Model architecture We consider time-continuous recurrent neural networks (RNNs) architecture that are commonly used to model neural circuits (Liu et al., 2024; Ehrlich et al., 2021). Specifically, we consider RNNs with 1 hidden layer, ReLU activation, N_{in} input units, N_{hidden} hidden units, and N_{out} output unit. Let $x_t \in \mathbb{R}^{N_{in}}$, $y_t \in \mathbb{R}^{N_{out}}$ be the corresponding input and output at time-step t . The model’s hidden representation h_t and outputs \hat{y}_t at time step t can be defined by the given equations:

$$h_{t+1} = \rho h_t + (1 - \rho)(W_h \sigma(h_t) + W_i x_t) \quad (\text{F.1})$$

$$\hat{y}_t = W_o \sigma(h_t) \quad (\text{F.2})$$

In the above equation, $W_i \in \mathbb{R}^{N_{in} \times N_{hidden}}$, $W_h \in \mathbb{R}^{N_{hidden} \times N_{hidden}}$, $W_o \in \mathbb{R}^{N_{hidden} \times N_{out}}$. $\sigma(\cdot)$ is the non-linear activation function, in which we used ReLU, and ρ is the decay factor which is defined by $\rho = e^{-\frac{dt}{\tau}}$ with time step dt and time constant τ . We use $N_{hidden} = 300$ for all RNNs models.

Weight rank initialization Following the practice in (Liu et al., 2024), we initialize the recurrence weight W_h by initializing an initial full-ranked random Gaussian matrix, and then use Singular Value Decomposition to truncate the weight rank to the desired rank. The truncated weight matrix is then re-scaled to ensure that weight matrices with varying ranks have the same weight norm.

F.1.3 Training Procedure

- Loss function: Since all three tasks that we consider are classification tasks, we use cross entropy loss.
- Optimizer: We use Stochastic Gradient Descent with momentum (implemented as `torch.optim.SGD(lr=0.003, momentum=0.9)`) to train the models.
- Batch size: We use batch size of 32 for each training step.

The models are trained for 10000 iterations and all models being compared achieved similar loss and accuracy after training (see Figure 18, 19, 20 for more details).

F.1.4 Manifold Capacity Measurements

In this section, we provide detailed information about how we define object manifolds from the model’s representations and measure the manifold capacity and geometric properties (Chung et al., 2018).

- Features extraction: We extract the representation h_t (in Equation F.1) from the hidden layer (dimension 300) with t being the decision period of the trial.
- Number of manifolds: The number of possible choices in the decision period of all the three tasks that we consider is 2, so the number of manifolds are 2.
- Number of points per manifold: For each task-relevant manifold, we randomly sample 50 trials of the corresponding ground truth choices.
- Number of repetitions: Every capacity and geometry measurement is repeated 50 times and we report the mean and the error bar as the bootstrapped 95% confidence interval calculated using `seaborn.lineplot(errorbar=('ci', 95))`.

F.2 Additional results on other cognitive tasks

In section 5.1, we present the results on how the initial structural connectivity bias (initialized by varying the rank of the weight matrix) affects the feature learning regime and representational geometry of a given model in the perceptual decision making task (also called the two-alternative forced choice task) (Britten et al., 1992). In this section, we show more detailed results (including accuracy and loss) on the perceptual decision making task in Figure 18, along with two other cognitive tasks, which are context decision making task (Mante et al., 2013) in Figure 19 and delay match sample task (Miller et al., 1996) in Figure 20.

Perceptual Decision Making Task

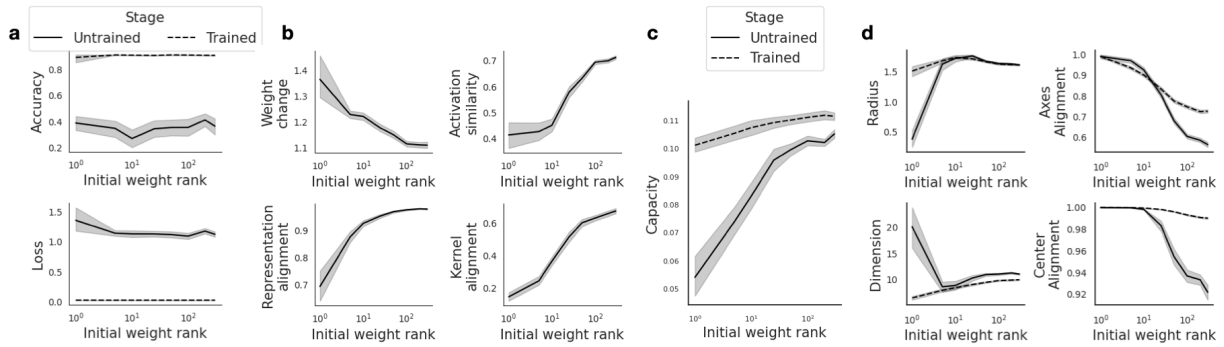


Figure 18: Structural connectivity bias in the two-alternative forced choice task. **a.** Model train and loss accuracy **b.** Weight change and alignment measurements **c.** Manifold capacity measurements **d.** Effective manifold geometry measurements.

Context Decision Making Task

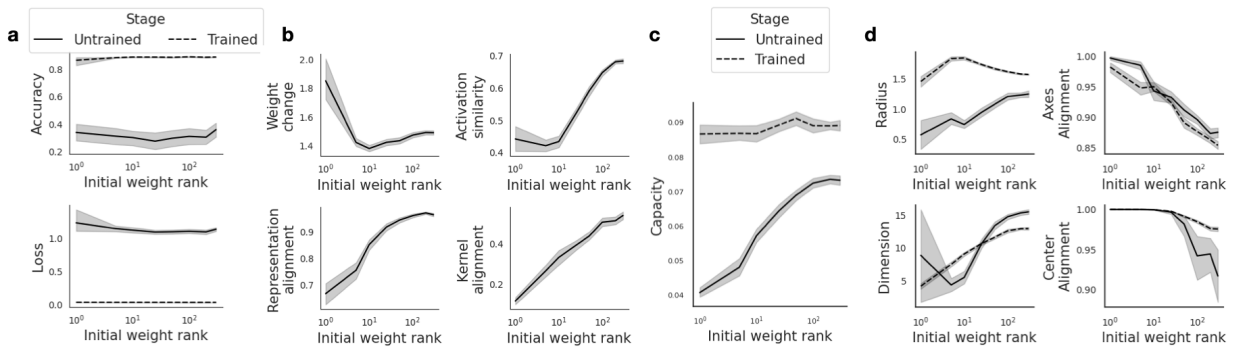


Figure 19: Structural connectivity bias in the context decision making task **a.** Model train and loss accuracy **b.** Weight change and alignment measurements **c.** Manifold capacity measurements **d.** Effective manifold geometry measurements.

Delay Sample Matching Task

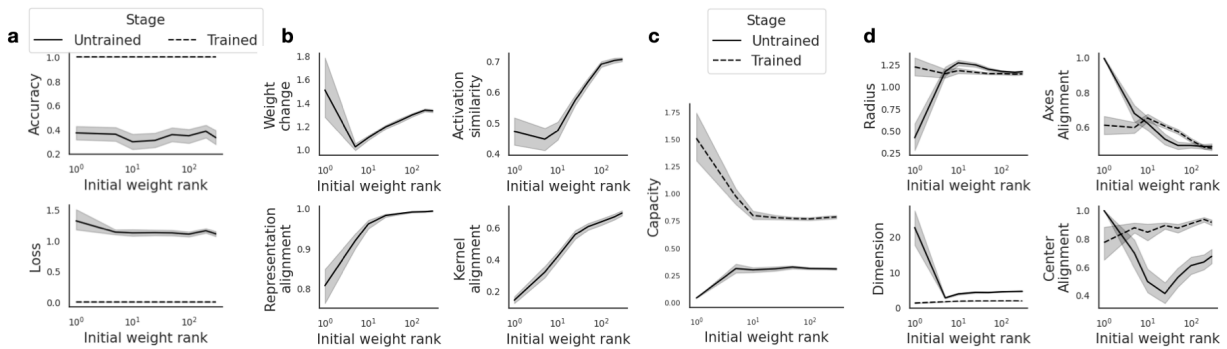


Figure 20: Structural connectivity bias in the delay matching sample task. **a.** Model train and loss accuracy **b.** Weight change and alignment measurements **c.** Manifold capacity measurements **d.** Effective manifold geometry measurements.